Multimode 3-D Kirchhoff Migration of Receiver Functions at Continental Scale

F. Millet, T. Bodin, S Rondenay

To cite this version:

F. Millet, T. Bodin, S Rondenay. Multimode 3-D Kirchhoff Migration of Receiver Functions at Continental Scale. Journal of Geophysical Research : Solid Earth, 2019, 10.1029/2018JB017288 . hal-02389074

HAL Id: hal-02389074
https://hal.science/hal-02389074v1

Submitted on 2 Dec 2019

JGR Solid Earth

RESEARCH ARTICLE
10.1029/2018JB017288

Key Points:

- We develop a fully 3-D teleseismic scattered waves imaging method that uses fast 3-D traveltime calculations
- Our method accounts for free-surface multiple scattering modes and polarity reversals for nonhorizontal interfaces
- Application of our method to field data in the Hellenic subduction zone yields images that are coherent with previous 2-D imaging results

Supporting Information:

- Supporting Information S1

Correspondence to:
F. Millet,
florian.millet@ens-lyon.fr

Citation:
Millet, F., Bodin, T., & Rondenay, S. (2019). Multimode 3-D Kirchhoff migration of receiver functions at continental scale. *Journal of Geophysical Research: Solid Earth*, *124*. https://doi.org/10.1029/2018JB017288

Received 31 DEC 2018
Accepted 19 JUL 2019
Accepted article online 4 AUG 2019

Multimode 3-D Kirchhoff Migration of Receiver Functions at Continental Scale

F. Millet[1,2], **T. Bodin**[1], **and S. Rondenay**[2]

[1]Laboratoire de Géologie de Lyon, UMR 5276, Université de Lyon, Villeurbanne, France, [2]Department of Earth Science, University of Bergen, Bergen, Norway

Abstract Receiver function analysis is widely used to image sharp structures in the Earth, such as the Moho or transition zone discontinuities. Standard procedures either rely on the assumption that underlying discontinuities are horizontal (common conversion point stacking) or are computationally expensive and usually limited to 2-D geometries (reverse time migration and generalized Radon transform). Here, we develop a teleseismic imaging method that uses fast 3-D traveltime calculations with minimal assumption about the underlying structure. This allows us to achieve high computational efficiency without limiting ourselves to 1-D or 2-D geometries. In our method, we apply acoustic Kirchhoff migration to transmitted and reflected teleseismic waves (i.e., receiver functions). The approach expands on the work of Cheng et al. (2016, https://doi.org/10.1093/gji/ggw062) to account for free surface multiples. We use an Eikonal solver based on the fast marching method to compute traveltimes for all scattered phases. Three-dimensional scattering patterns are computed to correct the amplitudes and polarities of the three component input signals. We consider three different stacking methods (linear, phase weighted, and second root) to enhance the structures that are most coherent across scattering modes and find that second-root stack is the most effective. Results from synthetic tests show that our imaging principle can recover scattering structures accurately with minimal artifacts. Application to real data from the Multidisciplinary Experiments for Dynamic Understanding of Subduction under the Aegean Sea experiment in the Hellenic subduction zone yields images that are similar to those obtained by 2-D generalized Radon transform migration at no additional computational cost, further supporting the robustness of our approach.

1. Introduction

Scattered phases in the coda of main teleseismic body-wave phases have been used to map discontinuities at various scales in the Earth. As opposed to direct phases that are mainly sensitive to volumetric heterogeneities, the scattered wavefield contains information about sharp structures that standard traveltime or surface wave tomography cannot resolve (Langston, 1979). The large amount of computations needed to exploit the scattered wavefield has limited its first applications to small-scale studies. However, there has been a growing interest to exploit the scattered wavefield at larger scale because the scattering structures are associated with variations in composition, mineralogical, or water content that are often linked to global scale phenomena. Exploiting these data in the form of receiver functions (RFs) sheds light on open research topics such as the dehydration of slabs (Tauzin et al., 2017), deep phase transitions in secondary minerals (Cottaar & Deuss, 2016), and the water content of the mantle transition zone (Zheng et al., 2007).

RF analysis extracts structural information from body-wave seismograms by removing the source component to retrieve the *P*-to-*S* and *S*-to-*P* converted waves (see, e.g., Bostock & Rondenay, 1999; Langston, 1979; Levander & Miller, 2012; Park & Levin, 2000). It is based on the separation between the signal of the incident wave and that of the scattered wavefield in seismograms recorded at teleseismic distances (Langston, 1979; Phinney, 1964). In the case of first-order forward *P*-to-*S* scattering at a horizontal interface, the incident wave is the direct *P* wave, and the scattered energy corresponds to an S_V wave that is mostly recorded on the radial component of the seismograms. The data are selected for epicentral distances ranging from 30° to 95° to avoid core phases and triplications from the mantle transition zone. The simplest way to exploit these *P*-to-*S* data is to deconvolve the vertical component from the radial. This assumes that the signal on the vertical component corresponds to the *P* wave and that it represents the source time function. This deconvolution removes the complexity associated with the source time function from the *S* waves on the radial component and thus produces a waveform that can be interpreted in terms of scattering structure. More advanced deconvolution methods optimize the source and noise estimates on three components for station arrays (Chen et al., 2010). Estimating a source time function in 3-D allows to get three component RFs that contain more information about the scattering structure than simple vertically deconvolved radial RFs.

Deconvolved teleseismic waveforms can be interpreted with common conversion point (CCP) stacking methods, which are a useful tool to obtain first-order images of the structure in the crust and upper mantle below an array of seismic stations (Dueker & Sheehan, 1997; Tessmer & Behle, 1988). By using a reference 1-D velocity model and applying lateral move-out corrections, these methods allow to project stacked scattering potential back at depth. These methods have been successfully applied to large data sets such as USArray in North America (Levander & Miller, 2012) and J-array/Hi-net in Japan (Yamauchi et al., 2003). Many of these CCP imaging methods only use the radial component of the RF, as it is faster and easier to interpret. Tonegawa et al. (2008) showed that the transverse component CCPs can also provide information about dipping reflectors. However, in the case of dipping structures, the polarity of *S* waves in the transverse component varies with back azimuth, and caution must be taken when stacking. This usually means that analysts restrain their data sets to convenient back azimuth directions where polarities are coherent.

CCP methods rely on the fundamental assumption that imaged structures are horizontal, which allows for fast move-out corrections and stacking. This assumption is clearly not valid in many geological settings such as subduction zones or orogens. Some approaches, such as the one-way wave equation migration (Chen et al., 2005), include 3-D filtering to effectively take lateral heterogeneities into account. More complex methods such as reverse time migration (RTM; Burdick et al., 2013) rely on an inversion that requires the numerical computation of full scattered waveforms for every source-receiver pair in a complex reference velocity model. Generalized Radon transform (GRT) migration includes amplitude-sensitive weights that recover 2-D or 3-D velocity anomalies (see, e.g., Bostock et al., 2001; Pavlis, 2011). These more sophisticated approaches treat the full scattered wavefield and hence use all three components of the RF. They are more accurate but also computationally more expensive and require higher data coverage than CCP. They are therefore usually limited to local-scale applications on dense linear arrays (Rondenay, 2009). As many geological settings tend to exhibit nearly 2-D geometries, imaging in 2-D is often sufficient to resolve subsurface structure accurately (see, e.g., Pearce et al., 2012). These methods have been applied successfully in complex tectonic settings such as the Tibetan plateau (Shang et al., 2017) or Cascadia subduction zone (Abers et al., 2009; Rondenay et al., 2001). An extensive review of scattered body-waves imaging techniques can be found in Rondenay (2009).

Until the last decade, the cost associated with 3-D migration was too prohibitive to develop fully 3-D imaging methods for scattered body waves. In recent years, however, the advent of new fast computational tools gave rise to a new generation of methods for imaging laterally varying structures over a range of scales. For example, a fully 3-D *P* wave coda waveform inversion has been proposed by Frederiksen and Revenaugh (2004) and is a promising tool for local to regional studies but remains computationally expensive. Two- and three-dimensional CCP approaches have also been devised to image laterally varying media at large scales and have been successfully applied to several regions in North America and Asia (Rondenay et al., 2017; Tauzin et al., 2016). Recently, Pavlis (2011) extended the GRT imaging principle to image 3-D structures. Wang and Pavlis (2016) used a plane wave approximation and performed ray tracing in a radially symmetric 1-D reference Earth model. This approach is certainly valid for looking at structures that are fairly continuous laterally, such as the mantle transition zone. However, it can be inadequate in regions where there are strong lateral variations in background seismic properties, such as subduction zones, where local focusing and defocusing effects can become predominant.

Cheng et al. (2016) took another approach and devised a 3-D migration method based on the Kirchhoff imaging principle, a well established method in exploration geophysics (Claerbout, 1985). It has been adapted for use with teleseismic data in the past decades (Ryberg & Weber, 2000) and is the basis for the regularized Kirchhoff migration (Wilson & Aster, 2005) and the GRT migrations (Bostock et al., 2001; Liu & Levander, 2013). In the data space (i.e., the time domain), teleseismic Kirchhoff imaging stacks the data along diffraction hyperbolae corresponding to an ensemble of arrivals consistent with a scattering point. In the model space (i.e., the depth domain), this is equivalent to mapping a given observed phase to an ensemble of grid points that predict the arrival time of that phase, that is, a migration isochron. By migrating all the waveforms along isochrons, and stacking over multiples source-receiver pairs, the structure can be recovered.

However, one of the drawbacks of this method is that the data coverage needs to be dense enough for the migration isochrons to stack up constructively.

What makes Kirchhoff migration attractive is that only the traveltimes of the scattered phases need to be estimated, instead of the complex scattered wavefield required by other methods (RTM and GRT). The advantage is that the traveltimes can be quickly computed by solving the Eikonal equation. We compute them using the fast marching approach with the FM3D software package developed by de Kool et al. (2006). Cheng et al. (2016) showed that a fully 3-D Kirchhoff prestack migration is computationally tractable. Their method was tested using 2.5-D synthetic data obtained from ray tracing (Raysum, Frederiksen & Bostock, 2000), as well as data from the Cascadia93, Mendocino, and USArray experiments. A similar method based on sensitivity kernels for P-to-S and S-to-P conversions has been devised by Hansen and Schmandt (2017) and tested using 2-D synthetics obtained from spectral element simulations (Specfem2D; Tromp et al., 2008). Both methods have the same order of computational cost as 2-D GRT and can image laterally varying structures such as subducting slabs given a dense ray coverage of the region of interest.

Here we extend the work of Cheng et al. (2016) on Kirchhoff prestack depth migration of teleseismic RFs with amplitude corrections from scattering patterns. We propose three improvements to this work. First, we migrate all three components of the recorded wavefield to enhance the coherence of the stack. Second, we incorporate the free-surface multiples in the migration algorithm. One of the problems that was highlighted in Cheng et al. (2016) is the presence of artifacts in the final image due to free surface multiples. These spurious signals might be misinterpreted as direct P-to-S conversions at the lithosphere-asthenosphere boundary (LAB). Here we address this problem by migrating the data a first time assuming that the arrivals correspond to a direct P-to-S conversion and three more times assuming the arrivals correspond to free surface multiples (i.e., surface backscattering). We use the fast marching method (FM3D software) to compute efficiently the traveltimes for any given reflected and transmitted phases combination. Third, we use fully 3-D scattering patterns to correctly treat all components (P, S_V, S_H) that are observed at the surface. Once the traveltimes are computed for all the scattered phases, one needs to account for the amplitude and polarity of these phases, which can vary in the case of nonhorizontal structures (Cheng et al., 2016; Tonegawa et al., 2008). The polarities and amplitudes are corrected using 3-D scattering patterns as those described in Beylkin and Burridge (1990). The scattering patterns can be seen as simulating the physics of elastic wave propagation without having to compute expensive scattered wavefields.

Similar to approaches discussed by Rondenay (2009), our new method initially generates one image per scattering mode, so four images in total. A final migrated image is then built by stacking these individual scattering mode images. We test three stacking techniques to enhance the structure that is most coherent between the forward and backscattered modes. We first try a linear stack between the four modes. Then we implement a phase-weighted stack, which acts as a phase coherence filter. Lastly, we implement a second-root stack that acts as an amplitude coherence filter.

In the following sections, we derive our improved 3-D Kirchhoff imaging approach and discuss its ability to resolve complex 2-D and 3-D structures. Here, we only describe the method for use with the P-to-S RF, but one could devise a similar method for use with S-to-P RF. After describing in detail the method in section 2, we test it in section 3 by conducting a series of synthetic tests using the Raysum software (Frederiksen & Bostock, 2000) in both artificially challenging and realistic scenarios. We show that a typical subduction zone structure can be retrieved. Finally, we test our method on a field data set from Greece in section 4.

2. Methodology

2.1. Three Component RFs

The radial, transverse, and vertical components of seismograms and RFs record different yet coherent responses to discontinuities in the and therefore provide complementary information about the structure of the Earth (see, e.g., Tonegawa et al., 2008). For horizontal interfaces and isotropic media, we know that the P-to-S conversions for a near vertical incidence are mostly recorded on the radial component. As RFs are usually computed for near vertical incidences of teleseismic waves in isotropic horizontally layer media, traditional studies consider only the radial component in the deconvolution. However, in the case of dipping interfaces, this energy is partitioned between the radial and transverse horizontal components. Moreover, because teleseismic arrivals are never truly vertical, some of the P-to-S energy is recorded on the vertical component, and some of the P-to-P and S-to-P conversions are recorded on the horizontal components.

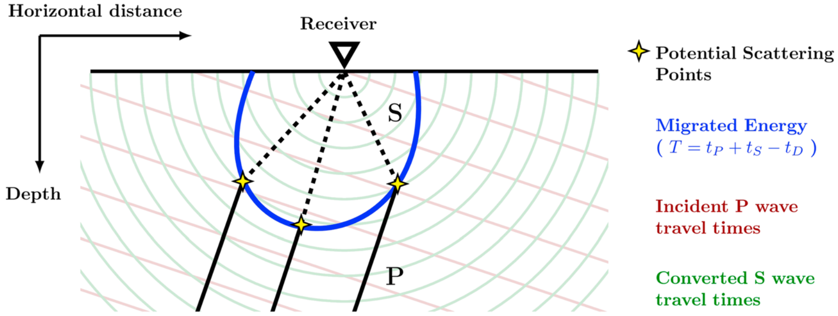

Figure 1. Schematic illustration of the 3-D Kirchhoff prestack imaging principle along a 2-D profile. The incoming *P* waves (solid lines, red background isochrone lines) and scattered *S* waves (dashed lines, green background isochrone lines) arrival times are computed at each grid point in the 3-D model box, and the energy is migrated (blue curve) along a differential isochron that corresponds to the time delay between the incident and scattered wave—that is, the difference in traveltime *T* between the direct wave (t_D) and the *P* wave to the scatterer (t_P) added to the *S* wave to the receiver (t_S). This isochron represents all the points in depth in the 3-D model space that could account for scattered energy seen at a given time on the receiver function. In the 3-D case, the isochron extends as an ellipsoid whose shape depends on the source-receiver geometry and the reference velocity model.

These effects are even stronger in the case of large volumetric velocity heterogeneities. In this study, we use three component teleseismic RFs, as we aim to properly account for effects of dipping interfaces and lateral variations in elastic properties.

For the synthetic cases presented below, we directly migrate the three-component waveforms obtained with the Raysum calculations, as they already correspond to the structural impulse response convolved with a Gaussian source time function. For the field data, we use a multichannel preprocessing approach similar to the one described in Rondenay (2009) to extract the scattered wavefield for each source. The three-component RFs at all the stations for each source are obtained by (1) estimating the source time function through principal component analysis on the *P* components of the $P - S_V - S_H$ rotated seismograms; (2) removing the source waveform $\bar{P}$ from the records to obtain the estimated three-component scattered wavefields $P' - S_V - S_H$, where $P' = P - \bar{P}$; and (3) deconvolving the estimated scattered wavefields by the estimated source wavefield in the frequency domain using a regularized least squares inversion with optimal damping parameter for each seismogram and each component (Bostock & Rondenay, 1999; Pearce et al., 2012).

2.2. Kirchhoff Prestack Depth Migration

In order to exploit these three-component RF signals, we implement a prestack migration that allows to naturally take 3-D effects into account. Kirchhoff prestack depth migration is a technique that was developed in exploration geophysics and that maps scattered phases observed on seismograms located at the surface back at depth to scattering points (see, e.g., Ylmaz, 2001). Using a reference velocity model, the energy is propagated back in depth to all the points in 3-D that would provide the same observed arrival. By doing so, we effectively treat each grid point as a potential scatterer and smear the energy of a given observed arrival along a migration isochron in the depth domain. The energy at depth for each observed trace is then stacked after migration. Alternatively, in the data space, this corresponds to finding the scattering points or interfaces by stacking the energy peaks along coherent diffraction hyperbolae. A visual representation of the Kirchhoff imaging principle in the model space is shown in Figure 1.

For two observed phases on two different waveforms corresponding to the same scattering point (i.e., on the same diffraction hyperbola), the depth-migrated isochrons will intersect at the actual scattering point and stack up constructively. Extending this observation to all source-receiver couples and all scattering points, one can see that this stacking in the depth domain will focus the energy from the isochrons to the actual scattering features. However, for this method to work correctly, a high density of data is required. For teleseismic data, an ideal array would have an interstation spacing of less than half the depth of the shallowest structure that we are interested in imaging (Rondenay et al., 2005). As summarized in Rondenay (2009), the imaging principle for the teleseismic Kirchhoff prestack depth migration can be written in general terms as

$$f(x) = \int\int \vec{\mathrm{w}}(x, r) \cdot \Delta\vec{\mathrm{u}}(r, t = T(r, x))\, dr, \tag{1}$$

where $f(x)$ is the scattering potential at a given image point x in depth, r describes the source-receiver geometry on the region of interest, the weights $\vec{w}(x, r)$ are linked to the treatment of the wavefield's amplitude and polarity during the migration, $\Delta\vec{u}$ is the three-dimensional scattered wavefield obtained through the multichannel preprocessing approach described in previous section with a $i\omega$ wavelet shaping factor applied in the frequency domain, and $T(r, x)$ represents the arrival times associated with a given (source-scatterer-receiver) geometry estimated in a reference 3-D velocity model. For the forward P-to-S scattering, for example, we have $T(r, x) = t_P + t_S - t_D$, where t_P, t_S, and t_D are traveltimes computed in the reference 3-D velocity model. t_P is the traveltime for the P wave traveling from the source to the scattering point, t_S for the S wave traveling from the scattering point to the receiver, and t_D for the direct P wave traveling from the source to the receiver. We use the fast marching method (FM3D, de Kool et al., 2006) to compute these traveltime fields. FM3D solves the Eikonal equation in our 3-D space after initializing the teleseismic arrival times at the border of the domain. It yields the traveltime fields for all the scattered phases, including the free surface multiples, by propagating the wavefield a first time upward (direct) and a second time downward (reflected). It uses this multistage approach to obtain all the traveltimes with only one computation. This makes this approach computationally efficient. The integration is carried out over all the sources and receivers.

The wavelet shaping factor ($i\omega$) must be applied to the scattered wavefield data $\Delta\vec{u}$ to account for the 3-D propagation of the wavefield in the Kirchhoff migration theory (Ylmaz, 2001). This means that instead of migrating the proper RF, we migrate its derivative. More precisely, the $i\omega$ factor transforms a Gaussian pulse on the RF into two consecutive pulses, the second one having the same polarity as the Gaussian and the first one the opposite polarity. These two pulses are at twice the frequency from the original signal and shifted by a half wavelength of the original signal, to earlier times for the first pulse and later times for the second one. This allows for the stacking to occur exactly on the interface where the second pulse is migrated and to reduce the noise above the interface through destructive interference with the first pulse.

The weights $\vec{w}(x, r)$ account for the amplitude of the migrated waveforms. They are a linear combination of the geometrical spreading, the scattering patterns, and the projection of the incoming polarization vector of the scattered phase on the (R, T, Z) reference frame at the station. Note that the reference frame changes for each event. The geometrical spreading accounts for amplitude reduction due to 3-D wave propagation from the scattering point to the receiver. The scattering patterns can be seen as simulating the physics of elastic wave propagation (e.g., amplitude of a P-to-S conversion) without having to numerically compute the full wavefield. These weights allow us to model the amplitudes of the scattered wavefield and to take into account amplitude information in the observed data. The application of the $i\omega$ shaping factor does not alter the amplitudes, as it amounts simply to a derivation of the signal (i.e., a linear operation).

2.3. Accounting for Scattering Theory

Cheng et al. (2016) showed that, in order to image dipping discontinuities for any incoming slowness and back azimuth, the polarities and amplitudes of the RF can be corrected by using scattering patterns. However, the authors used the scattering patterns from Rondenay (2009), which are 3-D scattering patterns projected in 2-D. This approximation is valid for S_V scattered waves that are polarized in the plane defined by the source, the scattering point, and the receiver (hereafter called the scattering plane) and is applicable to the case of forward P-to-S scattering. However, in order to treat the S_H waves generated by scattering of free surface reverberations, we need to use fully 3-D scattering patterns.

Scattering patterns describe the amplitude and orientation of the polarization vector of the wave scattered at any point x in our 3-D model space, for a given source-receiver geometry r. That is, for a given angle between the incoming and scattered wave, they give the amplitude and sign of the scattered phase. We compute this value for every r geometry and each possible scattering point x in our 3-D model. The projection of the estimated polarization vector from x to the station on the (R, T, Z) reference frame at the station is a measure of how much a scatterer at x would contribute to each component of the RF. Applying the dot product between this resulting vector and the observed wavefield $\Delta\vec{u}(r, t = T(r, x))$ tells us how much energy should be migrated to x.

As suggested in Tonegawa et al. (2008), migrating multiple component RFs improves the final image if polarities are correctly treated. Using three-component RFs gives rise to three possible situations regarding the coherence of the data. If a given grid point corresponds to an actual scatterer, we will extract coherent information on the three components of the RF. If the grid point corresponds to a geometry where no scattering is theoretically expected (e.g., a 180 angle between an incoming P and a scattered S wave), no energy will be migrated from the RF. Finally, if the grid point has high potential scattering values but the three components of the RF are not coherent, that is, there is no scattering at that point, recorded amplitudes will be migrated but will interfere destructively when stacked together. This allows us to consistently extract the coherent information of the RF. We will now explicitly describe the terms in $\vec{\mathrm{w}}(x, r)$ and how we modify the imaging principle to incorporate the free surface multiples.

2.4. Three-Dimensional Scattering Patterns

Three-dimensional scattering patterns have been derived by a number of authors (e.g., Frederiksen & Revenaugh, 2004; Wu & Aki, 1985). Here we employ the 3-D scattering patterns derived for a single-scattering point that were obtained by Beylkin and Burridge (1990). The authors describe the behavior of a plane wave propagating in a smooth velocity model that hits a scattering point. Extending the equations for volumetric scattering to point scattering under the single-scattering Born approximation, they express the amplitude and polarization of scattered waves for incoming unit vectors. This defines the following scattering patterns, $\epsilon^{X_1X_2}$, for any given incident X_1 and departing X_2 seismic wave at the scattering point:

$$\begin{aligned}\epsilon^{pp}(\theta) = \;& \frac{\delta\rho}{\rho_0}\left(1+\cos(\theta)+\frac{\beta_0}{\alpha_0}(\cos(2\theta)-1)\right)\\ &+2\frac{\delta\alpha}{\alpha_0}+\frac{\delta\beta}{\beta_0}\left(2\frac{\beta_0^2}{\alpha_0^2}(\cos(2\theta)-1)\right),\end{aligned} \tag{2}$$

$$\begin{aligned}\epsilon^{ps}(\theta) = \;& \frac{\delta\rho}{\rho_0}\left(\sin(\theta)+\frac{\beta_0}{\alpha_0}\sin(2\theta)\right)\\ &+\frac{\delta\beta}{\beta_0}\left(2\frac{\beta_0}{\alpha_0}\sin(2\theta)\right),\end{aligned} \tag{3}$$

$$\epsilon^{sp}(\theta) = -\epsilon^{ps}, \tag{4}$$

$$\begin{aligned}\epsilon^{s_Vs_V}(\theta) = \;& \frac{\delta\rho}{\rho_0}(\cos(\theta)+\cos(2\theta))\\ &+\frac{\delta\beta}{\beta_0}\left(2\cos(2\theta)\right),\end{aligned} \tag{5}$$

$$\epsilon^{s_Hs_H}(\theta) = \frac{\delta\rho}{\rho_0}\left(1+\cos(\theta)\right)+\frac{\delta\beta}{\beta_0}\left(2\cos(\theta)\right). \tag{6}$$

where α is the P wave velocity, β is the S wave velocity, ρ is the density, subscript $\cdot_0$ corresponds to the smooth reference model, δ corresponds to the local heterogeneity at the scattering point, and θ is the scattering angle between the incoming X_1 phase and the X_2 scattered phase in the scattering plane at the scattering point. A visual representation of the 3-D scattering patterns can be found in Figure 2. Here, we note that S_V is defined locally at the scattering point and is the part of the S wave that oscillates in the scattering plane, not in the great-circle plane. Conversely, S_H oscillates orthogonally to the scattering plane.

In the scope of this article, we will use fixed values for $\delta\alpha$, $\delta\beta$, and $\delta\rho$. More specifically, we use (1) $\delta\rho = 0$ in all equations, effectively removing the backscattering linked to jumps in density from our analysis; (2) $\delta\alpha = 0$ for the P-to-S and S-to-S scattering; and (3) $\delta\beta = 0$ for the P-to-P scattering. We have to resort to these arbitrary choices because our migration method does not rely on an inversion; hence, we cannot easily mitigate the individual contributions of variations in ρ, α, and β. Therefore, we decide to focus on the main parameter for each scattering configuration, with α variations preferred for outcoming P waves and β variations preferred for outcoming S waves (see, e.g., Bostock & Rondenay, 1999; Bostock et al., 2001) . This will be represented by subscript $\cdot_\beta$ and $\cdot_\alpha$, respectively, hereafter.

The scattering angle θ is estimated from the directions of propagation of the incoming and scattered waves at the grid point, which are obtained from the gradient of the wavefront given by the Eikonal solver. The angle θ is used to estimate the amplitude and polarity of the scattered wave (equations (2) to (6)). This polarization vector is then projected on the (R, T, Z) reference frame at the station, thus resulting in a predicted amplitude vector $\vec{\mathrm{w}}(x, r)$. The level of coherence between the observed waveforms and amplitudes

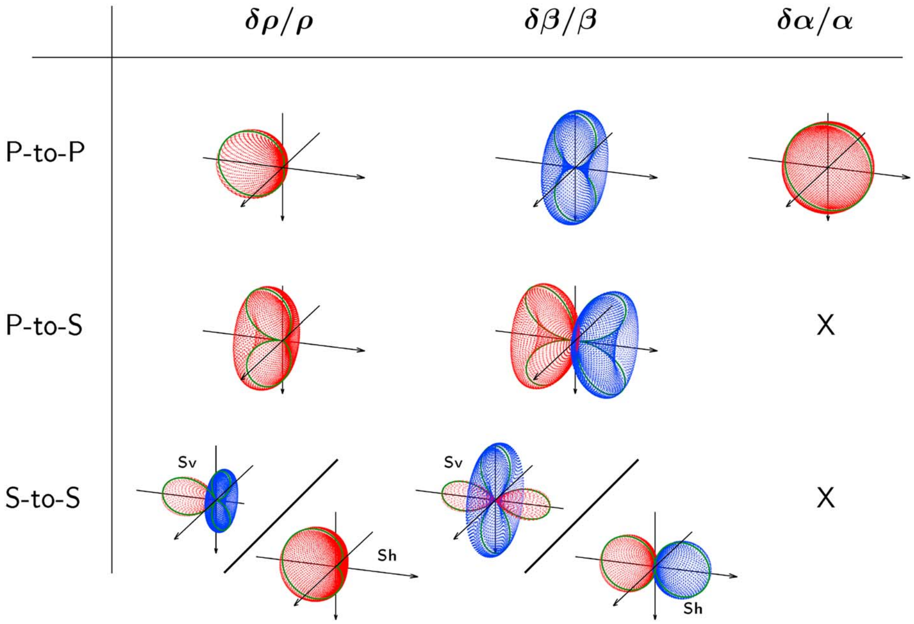

Figure 2. Representation of the 3-D scattering patterns. The incoming wave arrives from the left-hand side along the horizontal axis as either a *P* wave oscillating rightward or an *S* wave oscillating upward and leaves according to the scattering geometry. The scattering amplitude is represented as distance to the scattering point (center of each plot), and the polarity is represented by color, red being positive and blue negative. Here we can take both forward and backscattering into account. All of them are symmetrical with respect to the horizontal incoming wave propagation axis. Note that ρ perturbations generate mostly backscattering and α-β perturbations have equal parts of forward and backscattering. The final value for a given scattering geometry is obtained by multiplying the amplitude value by the polarity for that scattering angle.

predicted from the scattering geometry is measured by computing the dot product of the recorded energy vector $\Delta\vec{u}(r, t = T(r, x))$ and the predicted energy vector $\vec{w}(x, r)$ from the surface projection. This tells us how much energy scattered at point x is expected to contribute to each component of the RF and thus defines the level of recorded amplitude that is migrated to depth.

2.5. Forward Scattered Waves and Free Surface Backscattered Multiples

Standard RF studies interpret the phases observed in deconvolved waveforms only as forward *P*-to-*S* or *S*-to-*P* conversions, referred to as *PS* and *SP* hereafter, although a well-known issue is the influence of the free surface multiples (Lekić & Fischer, 2013; Levander & Miller, 2012). Interferences from these multiples can stack up at spurious depths and can generate serious artifacts that hinder the interpretation of features in the migrated images (Cheng et al., 2017). However, if properly accounted for, multiple reflections can become useful, as they bring complementary information about the structure (see, e.g., Tauzin et al., 2016).

The free surface multiples are the waves that reflect at the surface of the Earth and are then backscattered toward the surface by the same heterogeneities that generate the direct *PS* scattering. In the case of the Born approximation, we are looking at three different modes. The first one to arrive is reflected as a *P* wave at the surface, hereafter referred to as lower case *p*, and backscattered as a *P* wave. The second one is also reflected as a *P* wave but backscattered as an *S* wave toward the station. The third one is reflected as a converted *S* wave at the surface, hereafter referred to as lower case *s*, and backscattered as an *S* wave. These phases will be referred to as *PpP*, *PpS*, and *PsS*, respectively. Note that the *S*-to-*S* scattering for the *PsS* wave has as both an S_V-to-S_V and an S_H-to-S_H component.

In the next section we will show how these phases reflected at the surface (i.e., *PpP*, *PpS*, and *PsS*) are accounted for in the migration algorithm. Let us first write the imaging principle in the case of forward *PS* scattering mode. Since we work with a finite number of sources i and stations j and use a finite number of grid points k, equation (1) can be rewritten in a discrete form:

$$f_{ps}(k) = \sum_{i} \sum_{j} \mathrm{G}(j, k)\, \varepsilon^{ps}(i, j, k)\, \vec{\delta}_{ps}(j, k) \cdot \Delta\vec{u}(i, j, t_P + t_S - t_d), \tag{7}$$

where $f_{ps}(k)$ is the scattering potential for the forward *PS* scattering mode at a given grid point k, $\mathrm{G}(j,k) = 1/d(j,k)$ is the amplitude correction for geometrical spreading with $d(j,k) = |x(k)-r(j)|$ the distance between the receiver and the scatterer, ε^{ps} and $\vec{\delta}_{ps}$ represent the amplitude and polarization of the scattered *S* wave given by the scattering pattern for the *PS* mode (equations (3)). Finally, t_P, t_S, and t_D are traveltimes computed in the reference 3-D velocity model described in the previous section. We use the fast marching method (FM3D, de Kool et al., 2006) to compute these traveltime fields.

2.6. Integration of Free Surface Multiples

To incorporate the scattering modes from free-surface multiples in the migration and map their energy back at the correct location, we must compute their associated traveltimes and amplitudes corrections. Specifically, we need to compute the traveltimes for the initial *P* wave from the source to the surface, the reflected downward going *P* and *S* waves, and the backscattered *P* and *S* waves from all the grid points to the receivers. Again, we use the fast marching method to compute three traveltime fields (*P*, *Ps*, and *Pp*) for each source and two (upgoing *P* and *S*) for each receiver. By combining these *Pp* and *Ps* traveltimes with the *P* and *S* scattered wave traveltimes, we get the traveltimes for all modes.

We use the scattering patterns described above to get the amplitudes and polarities for these modes as well. However, in the case of the free surface multiples, the behavior of the amplitude and polarity of the phases is more complex than a single scattering pattern. In this case, we combine the appropriate $\varepsilon^{X_1X_2}$ scattering patterns in a complete, phase-specific scattering pattern S_m, where m represents one of the four scattering modes. We effectively treat the multiples as a double-scattering problem with one of the scattering being a reflection at the free surface of the Earth and the other the scattering at depth. Note that the reflection at the free surface is not a scattering per se, as the surface is seen as a horizontal discontinuity, and only one direction is possible for the reflected wave. This way we are still in the Born approximation and in a single-scattering regime.

The expressions for all the S_m can be found hereafter and are illustrated along migration isochrons in Figure 3. To obtain the sections in Figure 3, we first computed the theoretical arrival times for all modes associated with a 100-km deep horizontal discontinuity. We then created independent synthetic waveforms for all modes by generating a positive unit Gaussian pulse centered on these arrival times. Finally, we migrated these waveforms independently according to their respective complete scattering pattern for each mode. This figure shows how the scattering patterns allow to invert the polarity of the incoming phases independently for each mode and on each component. This is particularly visible on the radial and vertical components of the *PpS* mode. The complete scattering patterns are as follows:

$$S_{ps} = \varepsilon_{\beta}^{ps}(\theta), \tag{8}$$

$$S_{ppp} = \varepsilon_{\alpha}^{pp}(\theta')\ \varepsilon_{\alpha}^{pp}(\theta), \tag{9}$$

$$S_{pps} = \varepsilon_{\alpha}^{pp}(\theta')\ \varepsilon_{\beta}^{ps}(\theta), \tag{10}$$

$$S_{pss} = \varepsilon_{\beta}^{ps}(\theta')\ \left((\vec{\delta}' \cdot \vec{\delta})\ \varepsilon_{\beta}^{s_V s_V}(\theta) + (\vec{\delta}' \cdot \vec{\gamma})\ \varepsilon_{\beta}^{s_H s_H}(\theta) \right). \tag{11}$$

For the *PS* scattering this simply corresponds to the direct scattering pattern restricted to the $\delta\beta/\beta$ contribution. In contrast to the direct *PS* scattering mode, there are two scattering angles to consider for the multiples. The first one is the angle θ' at the free surface reflection, which is the angle of the incident wave in the great circle plane that contains the source and the scattering point. The second one is the angle θ at the scattering point, which is in a second scattering plane defined by the free surface reflection point, the scattering point, and the receiver. Moreover, for the *S*-to-*S* scattering in the *PsS* scattering mode, we have to consider the polarization of the wave. In this case, δ' is the polarization of the wave that is reflected at the surface along the great circle path. This reflected wave is scattered partly as an S_V wave along δ and partly as an S_H wave along γ, which is orthogonal to δ. This leads to a generalized definition of the imaging principle, derived from equation (7), for every scattering mode:

$$f_m(k) = \sum_i \sum_j \mathrm{G}(j,k)\ \mathrm{S}_m(i,j,k)\ \vec{\delta}_m(j,k) \cdot \Delta\vec{\mathrm{u}}(i,j,T_m), \tag{12}$$

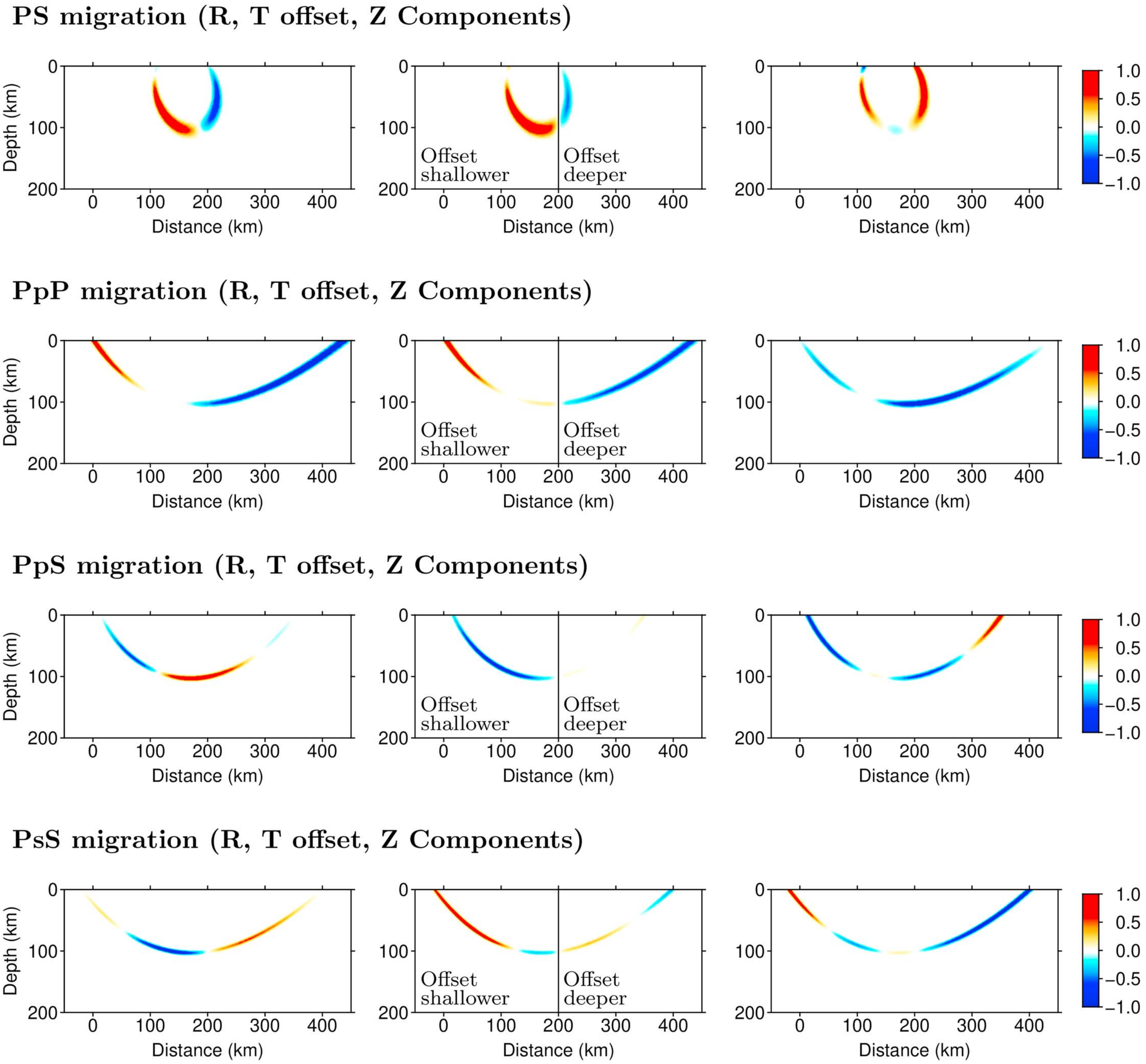

Figure 3. Two-dimensional representation of the complete scattering weights, without focusing, for the four scattering modes and the three-component migration. These are obtained by migrating a unit Gaussian pulse along the isochron for a given scattering mode for a source that arrives under the station from the right-hand side. They correspond to the projection of the weights from the scattering patterns at the surface for each recorded component, with blue corresponding to a polarity reversal and red to a preserved polarity. Each row corresponds to a different scattering mode, and the columns correspond to the three components of the recorded wavefield. For the transverse component, because its amplitude is null along the great circle plane, the slice through the 3-D model is offset shallower (toward the reader) or deeper (away from the reader) to better visualize its amplitude and polarity behavior. This is what produces the visible polarity reversals at 200 km.

where $f_m(k)$ is the scattering potential for the scattering mode m at the grid point k, $m \in [1,4]$ represents one of the four the scattering modes (either PS, PpP, PpS, or PsS), $\mathrm{S}_m(i,j,k)$ is the complete scattering pattern for a given m mode, $\vec{\delta}_m(j,k)$ is the unit polarization vector of the scattered wave arriving at the receiver for a given m mode, and T_m corresponds to the traveltime estimated in a reference 3-D model for a given m scattering mode. In the case of the PpP phase, this corresponds to $T_{PpP} = t_P(i,x') + t_p(x',x) + t_P(x,j) - t_D$ with x' denoting the surface reflection point and x the potential scattering point.

Since estimating the exact direction of polarization $\vec{\delta}_m(j,k)$ of the scattered wave at the receiver requires considerable extra computational cost, here we assume that the polarizations do not change from the scattering point k to the receiver j at the surface. This is equivalent to assuming straight rays in a homogeneous medium from the scattering point k to the receiver j. It is a reasonable approximation for lithospheric and upper mantle investigations but may represent an oversimplification for lower mantle studies, where the variations in elastic property bend the rays significantly before they reach the surface.

An additional weight is applied to the data in order to limit the contribution of long-distance interactions at shallow depths as they leak significant amounts of energy into the images above the region of interest and blur the images. This means that we effectively put a sensitivity region below the receivers that minimizes the arrivals with large incidence angles. Cheng et al. (2016) proved that this kind of sensitivity function helps remove artifacts in the migrated images. However, this means that we limit our ability to image steeply dipping reflectors. For the PS migration, this limits the dip of recoverable structures to 45°, and for the free surface multiples, it means that we lose sensitivity above ∼30° dip. To down-weight our data, we use a fourth-power cosine function of the incidence angle that provides a sharp roll-off at an angle of 45°, leading to the following updated expression for our imaging principle:

$$f_{m,foc}(k) = \sum_i \sum_j \mathrm{F}(j,k)\, \mathrm{G}(j,k)\, \mathrm{S}_m(i,j,k)\, \vec{\delta}_m(j,k) \cdot \Delta\vec{\mathrm{u}}(i,j,T_m), \tag{13}$$

where $f_{m,foc}(k)$ is the focused scattering potential for the scattering mode m at the grid point k, $F(j,k)=\cos^4(\nu)$ is the focusing factor, and $\nu(j,k)$ is the incidence angle of the scattered wave under the station. This factor can be set to 1 if one wants full coverage of possible dip angle resolution.

Using this imaging principle, we get four separate images, one for each scattering mode. In every image, the energy migrated from the waveforms due to one of the scattering mode is back propagated at the correct depth, while the other three modes are migrated at spurious depths. However, the benefit of this approach is that these spurious features are migrated at different positions in each image, whereas real structure will be at coherent depths over all modes. This means that extracting the coherent information between these four images should penalize against spurious features and enhance true structures.

2.7. Image Stacking Techniques

To enhance the structure that is most coherent between the forward and backscattered modes, we implement and test three stacking techniques: linear stacking, phase-weighted stacking (PWS), and second-root stacking. The phase weighted stack uses a measure of the coherence of the phases of all the migrated signals, whereas the second-root stack acts as an amplitude coherence filter. The following sections describe each of these techniques.

2.7.1. Linear Stacking

The first stacking technique is a linear stack over the four modes and can be summarized in the following equation:

$$f_{lin}(k) = \sum_m \sum_i \sum_j \mathrm{F}(j,k)\, \mathrm{G}(j,k)\, \mathrm{S}_m(i,j,k)\, \vec{\delta}_m(j,k) \cdot \Delta\vec{\mathrm{u}}(i,j,T_m), \tag{14}$$

where $f_{lin}(k)$ is the stacked scattering potential for all four modes at the grid point k.

As expected, this stacking scheme will enhance the features that are coherent across all four modes. However, since the sum is linear, we also expect the spurious features to be reduced by less than an order of magnitude if all modes have roughly the same migrated amplitude. This means that the spurious features will still be visible on the final image.

2.7.2. Phase-Weighted Stacking

The second technique we consider is PWS. In this approach, we compute the instantaneous phase $\varphi(t)$ of the input RF signals based on their analytical signals (Costa et al., 2018; Schimmel & Paulssen, 1997). We then migrate and stack the complex phase $e^{i\varphi_k(x)}$ at each grid point and take the norm of the stacked complex phase as a measure of the coherence (Cooper, 2009). This can be summarized in the following general equation:

$$y(x) = \frac{1}{N}\sum_{j}^{N} s_j(x) \left| \frac{1}{N}\sum_{k}^{N} e^{i\varphi_k(x)} \right|, \tag{15}$$

where the first sum represents the amplitude stack of the data s_j, the second sum is the norm of the stacked migrated complex phases $e^{i\varphi_k}$ that acts as a filter to the amplitude stack, and $y(x)$ is the stacked migrated signal. On one hand, if the signals are coherent, their instantaneous phases φ_k will point in the same direction, and the modulus of the sum of the complex phases will be high. On the other hand, if the signals at a given grid point consists mainly of noise, then the instantaneous phases will point toward random directions and cancel out, leading to a minimum in the modulus of the stacked complex phases.

In our case, we need to compute the instantaneous phase of the 3-D incoming signal using the estimated polarization of the scattered waves, which is different at every grid point, based on the instantaneous phase of the three components of the RF. This leads to a reformulation of our imaging principle as follows:

$$f_{pws}(k) = \mathrm{C}(k) \sum_{m}\sum_{i}\sum_{j} \mathrm{F}(j,k)\ \mathrm{G}(j,k)\ \mathrm{S}_m(i,j,k)\ \vec{\delta}_m(j,k)\cdot\Delta\vec{\mathrm{u}}(i,j,T_m), \tag{16}$$

where $f_{pws}(k)$ is the phase-weighted stacked scattering potential for all four modes at the grid point k. $\mathrm{C}(k)$ is the coherence of the four modes defined as

$$\mathrm{C}(k) = \left| \sum_{m}\sum_{i}\sum_{j} e^{i\varphi(m,i,j,k)} \right| \tag{17}$$

with

$$\varphi = arg(\mathrm{S}_m\ \vec{\delta}_m\cdot\Delta\tilde{\mathrm{u}}),$$

where $\Delta\tilde{\mathrm{u}}$ is the analytical signal of $\Delta\vec{\mathrm{u}}$.

2.7.3. Second-Root Stacking

Finally, we consider a second-root stacking technique based on Schimmel and Paulssen (1997). This is a nonlinear stacking method that sums the square root of the amplitudes for all the traces and takes the resulting image to the power of 2 after the stack. The general formula for Nth-root stacking can be summarized as follows:

$$y(x) = sign\,(r(x))\ \ |r(x)|^n \tag{18}$$

with

$$r(x) = \frac{1}{N}\sum_{j}^{N} sign\left(s_j(x)\right)\ \ |s_j(x)|^{1/n},$$

where $r(x)$ is the stack of the Nth roots of the $s_j(x)$ data and $y(x)$ is the final stacked migrated signal taken to the Nth power. We tried other power values for the Nth-root stacking method, but higher values tend to remove everything but the sharpest coherent contrasts, which can be problematic for smaller coherent scattering structures.

In our case, if we assign the variable $\mathcal{A}(i,j,k)$ to the corrected amplitude for every (i,j,k) triplet and the variable $\mathcal{S}(k)$ to the value of the stacked square root of the amplitudes at grid point k, we can rewrite our imaging condition as

$$f_{2rs}(k) = \mathrm{sign}(\mathcal{S}(k)) \left| \sum_{m}\sum_{i}\sum_{j} \mathrm{sign}(\mathcal{A}(i,j,k))\,|\mathrm{F}(j,k)\,\mathrm{G}(j,k)\,\mathrm{S}_m(i,j,k)\,\vec{\delta}_m(j,k)\cdot\Delta\vec{\mathrm{u}}(i,j,T_m)|^{1/2} \right|^2, \tag{19}$$

where $f_{2rs}(k)$ is the second-root stacked scattering potential for all four modes at the grid point k.

In the current section we described the physics and the geometry of the problem with the scattering patterns. We explicitly described the equations and the imaging principles we need to obtain the final stacked images of the subsurface. In what follows, we use synthetic examples to show that the resulting imaging principle (equation (13)) is robust and that we are able to integrate all the available data in the analysis without back azimuth or slowness restrictions. Then we show how the different stacking methods affect the results, and finally, we discuss the computational efficiency of the method and apply the imaging principles to real data.

Table 1
Synthetic Models and Setups

Model ID	Thickness (km)	Dip	V_P (km/s)	V_S (km/s)	Sources	Receivers
WCS1	200	0°	8.0	5.0	4	451
	∞	40°	8.8	5.5		
WCS2	100	0°	8.0	5.0	24	451
	∞	10°	8.8	5.5		
R2DSZ	40	0°	5.8	3.5	24	451
	110	0°	8.5	4.8		
	10	30°	5.8	3.5		
	30	30°	9.5	5.2		
	∞	30°	8.5	4.8		
MRT	40	0°	6.0	4.0	52	35
	60	0°	6.6	4.4		
	∞	20°	7.2	4.8		
MPKDM	20	0°	6.2	3.6	52	35
	20	0°	6.8	3.8		
	20	0°	7.6	4.2		
	∞	0°	8.0	4.5		

Note. Dip corresponds to the upper interface of the layer. The "∞" corresponds to the half-space at the bottom of the model. Thickness is taken at the center of the model and corrected for dip.

3. Synthetic Tests

Here we conduct a series of tests on three synthetic models that we designed to show how including scattering patterns, three component RFs, and free-surface multiples in the migration improves the final images. The synthetic models and test geometries are described in Table 1 and hereafter. The experimental setting for the third synthetic scenario (R2DSZ) is shown in Figure 4.

3.1. Model and Setup

3.1.1. Synthetic Models

The first model WCS1 comprises two layers separated by an interface with contrasts of 10% in α, β, and ρ at a 40° dip. This first synthetic model was designed to represent a typical challenging scenario where amplitude and polarities of the data strongly vary with epicentral distance and back azimuth. In this case, the polarity reversals that arise from steep arrivals on dipping discontinuities need to be addressed to correctly interpret the data (Cheng et al., 2016).

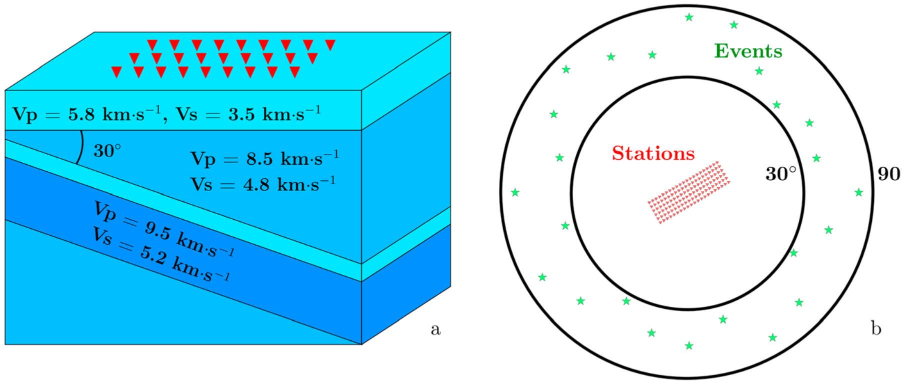

Figure 4. Synthetic setup for the tests in Figures 5 to 9. Red triangles represent the stations in the array, and green stars represent the events. The array is elongated in the along-dip direction, and the sources are evenly spaced in back azimuth and assigned a random epicentral distance from 30° to 90°. (a) is a block diagram that represents the velocity model for Figure 9 (cf. Table 1). (b) is a map view of the array and shows the event distribution for the tests performed in Figures 7 to 9. For enhanced clarity only half the rows and half the columns of the array are represented, and figures are not to scale.

Table 2
Index of Migrated Sections With the Effects Taken Into Account for Each

Fig.	Element	Components	Scat. patterns	Multimode	Sources	Additional proc.
5	a/b/c	R	No	No	1–2	No
	d/e/f	R	Yes	No	1–2	No
6	a/b/c	R	No	No	1–2	No
	d/e/f	T, Z	No	No	1–2	No
	g/h/i	R, T, Z	Yes	No	1–2	No
7	a/b/c/d	R, T, Z	Yes	No	24	No
8	a/b/c	R, T, Z	Yes	Yes	24	No
9	a/b/c/d	R, T, Z	Yes	No	24	No
	e/f/g	R, T, Z	Yes	Yes	24	No
10	a/b/c	R, T, Z	Yes	Yes	24	No
12	a	R, T, Z	Yes	Yes	52	No
	b/c/d	R, T, Z	Yes	Yes	52	Yes
13	a	R, T, Z	Yes	Yes	52	No
	b/c/d	R, T, Z	Yes	Yes	52	Yes

Note. Additional processing corresponds to the projection of the stations along the imaging line in the case of the Multidisciplinary Experiments for Dynamic Understanding of Subduction under the Aegean Sea experiment.

The second synthetic model WCS2 represents a worst-case scenario in terms of the influence of the free surface multiples. It has the same elastic contrasts and a 10° dip, and in this case we expect the free surface multiples to have a strong contribution in the migrated image for the *PS* mode.

The third model R2DSZ comprises five layers and represents an idealized 2-D subduction zone. The first layer is a 30-km-thick overriding crust. The second layer is the overriding mantle. The third and fourth layers are the subducting crust and lithospheric mantle that form the subducting plate, with respective thickness of 10 and 30 km and dipping at a 30° angle. The last layer is the unperturbed mantle under the subducting plate.

The synthetic waveforms are calculated in the sharp models for models containing sharp interfaces. Conversely, the traveltimes used to migrate these data are computed in a smoothed version of these models, with a 10-km buffer around the discontinuities, in order to emulate reference models obtained through local or regional tomography.

3.1.2. Synthetic Setup

In order to demonstrate that our migration method can be applied at continental scale, we test it on a synthetic array that spans 100 by 400 km (Figure 4). The array comprises 11 × 1 regularly spaced stations, with station spacing of just above 10 km. The sources are regularly spaced in back azimuth, that is, every 90° for WCS1/WCS2 and every 15° for R2DSZ. They are given a random epicentral distance from the center of the array between 30° and 90°. For R2DSZ, this simulates arrivals from a realistic range of slownesses and back azimuths. We acknowledge that this is an idealized geometry that is rarely available with field data as arrays usually have irregular shapes and sample an irregular distribution of back azimuths. We used up to 24 sources and created a total of up to 10,824 synthetic waveforms for each synthetic velocity model.

For the models WCS1 and WCS2, applying the successive imaging principles will help us demonstrate the improvements offered by three component RFs and correcting for scattering patterns. For the realistic 2-D subduction (Model R2DSZ), we expect this setup to image the overriding and subducting crust as a clear positive peak. We also expect the method to resolve both the crust and the LAB of the subducting slab.

3.1.3. Synthetic Waveforms

The synthetic data are generated with a ray-based approach for modeling teleseismic body waves in dipping anisotropic structures (Raysum software; Frederiksen & Bostock, 2000). This approach computes the arrival times and amplitudes of all converted and reflected (i.e., first-order free surface multiples) phases in a layered geometry. The advantage of this algorithm is that it is accurate and computationally efficient, No scattering patterns, R Component (down-dip, up-dip, both)

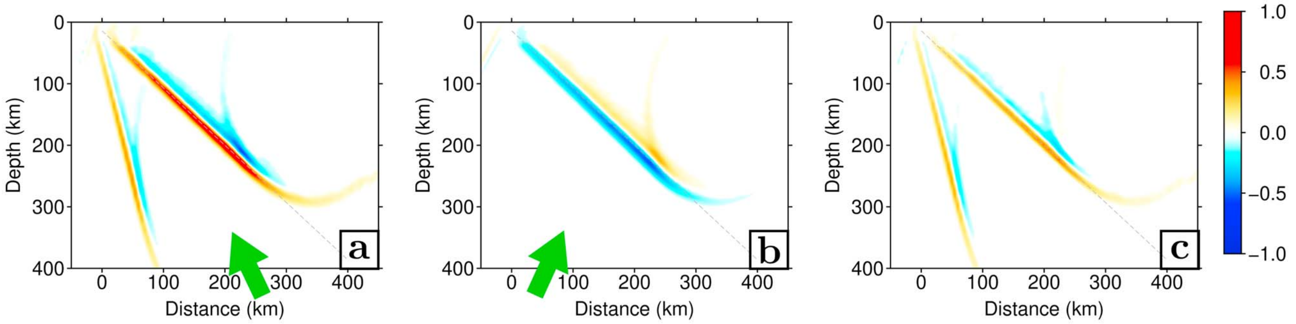

Scattering patterns included, R Component (down-dip, up-dip, both)

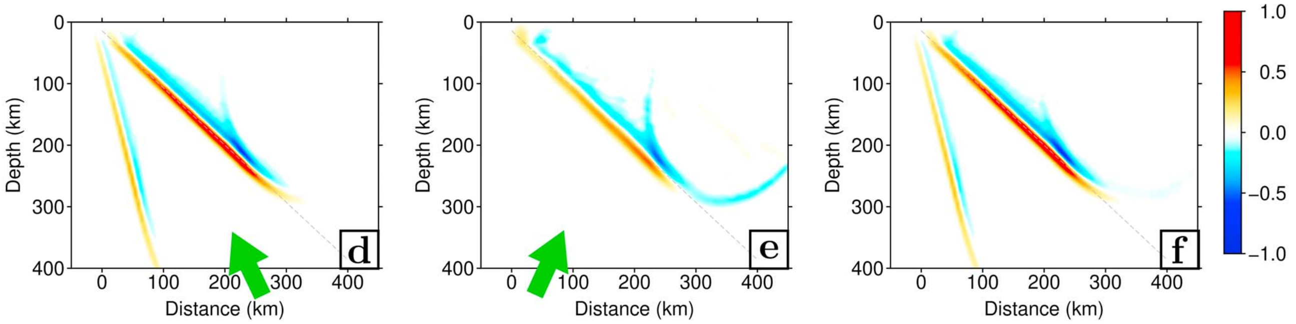

Figure 5. Influence of the scattering patterns. *PS* migration of radial receiver functions for a 2-D model containing a single interface with 40° dip and 10% δV_P, δV_S, and $\delta\rho$ perturbations (Model WCS1; Table 1). Arrows represent the direction of propagation of the incoming waves. (a) and (d) correspond to a downdip source coming from the right-hand side, (b) and (e) to an updip source coming from the left-hand side, and (c) and (f) correspond to the stacks of (a + b) and (d + e), respectively. (a) to (c) are migrated without the scattering patterns and show inconsistency in the migrated polarity. (d) to (f) are migrated with the effects of scattering patterns taken into account and show consistent polarity, which improves the stacked image.

as it uses analytical formulae to compute the traveltimes, amplitudes, and phase of the transmitted and scattered waves.

The Raysum software can handle a large number of planar, homogeneous anisotropic layers with arbitrary strikes and dips. However, the models cannot contain velocity or anisotropy gradients inside the layers, and the layers themselves cannot intersect in regions that are traversed by rays. Because of these limitations, we could not simulate a laterally limited slow mantle wedge in our idealized subduction zone model. Since our simulations cannot reproduce fully 3-D conditions, we will refer to them as 2.5-D synthetics hereafter.

Raysum outputs a sum of dirac delta functions convolved with a Gaussian source time function with a variable standard deviation, set to 3 s in our case. We use these data directly as our RFs, without noise, as our source function is already a Gaussian pulse.

3.1.4. Overall Computational Cost

The Eikonal solver estimates the traveltimes of scattered waves through a cube of 6° × 6° in latitude and longitude and 500 km in depth. Our migration is performed in a cube of 5° × 5° by 450-km depth to account for potential edge effects in traveltime calculations. The computations and migrations for all the synthetic cases were carried out on a single core of an Intel Xeon E5-2650 v2 octa-core processor. The Raysum and analytical signal computation take under 2 min to run. The exact number of sources and receivers used for every model, for synthetic and field data, are detailed in Table 2. Running FM3D for 24 sources and 451 receivers takes 3 hr with a voxel size of 5 × 5 × 5 km, on average. The migration of the 10,824 RF with the multimode algorithm also takes 3 hr to run. The memory requirements for the case just described are approximately 12 Gb. This includes the three time tables per source, namely, the upgoing direct *P* and downgoing *Pp* and *Ps* wavefields; the two time tables per receiver, namely, the upgoing scattered *P* and *S* wavefields; and the waveforms for all source-receiver pairs. For the smaller experiments on models WCS1 and WCS2, it takes 15 min and 1 hr to run all steps.

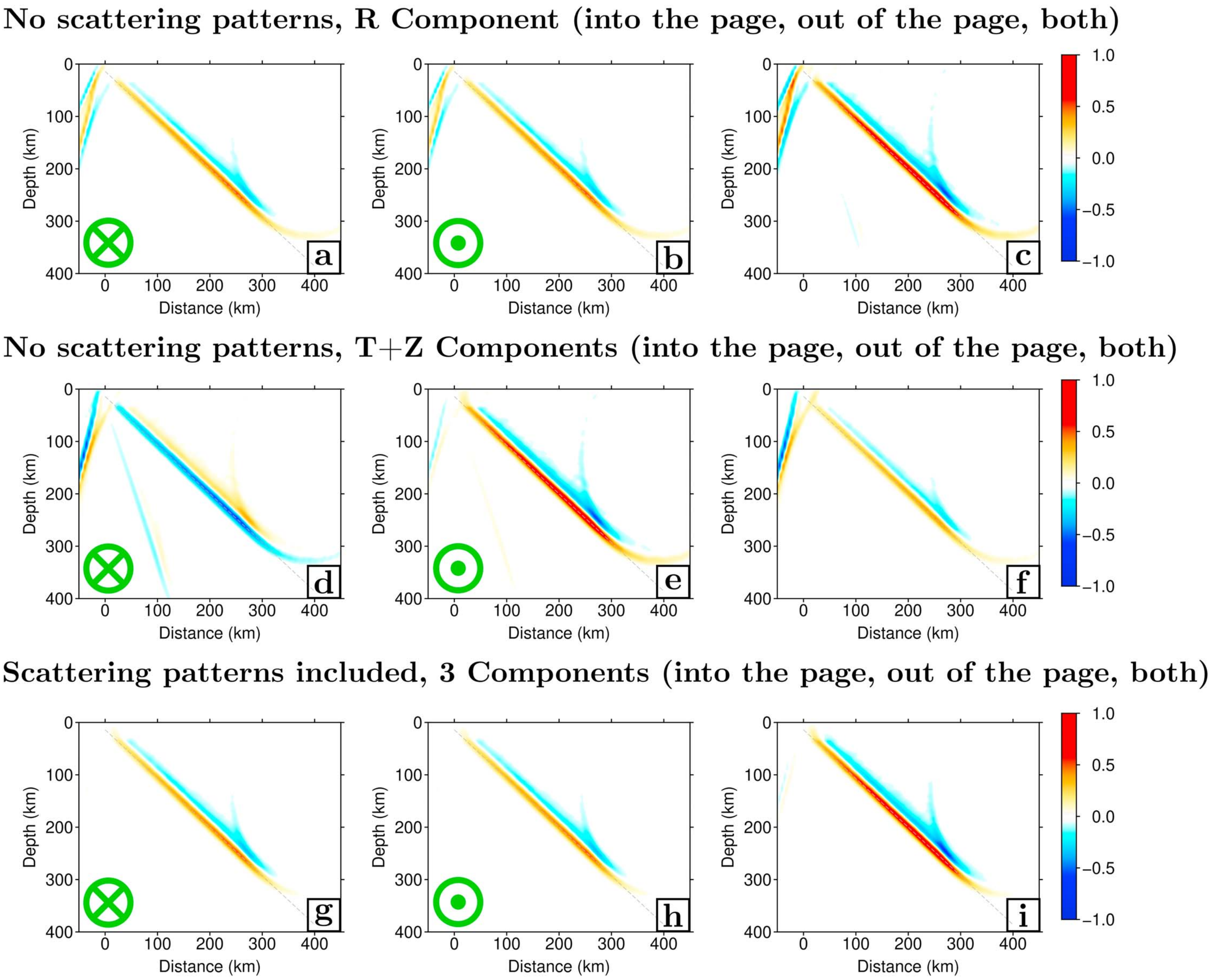

Figure 6. Influence of the three component migration. *PS* migration for a 2-D model containing a single interface with 40° dip and 10% δV_P, δV_S, and $\delta\rho$ perturbations (Model WCS1; Table 1). Symbols represent the direction of propagation of the incoming waves. (a), (d), and (g) correspond to an along-strike source coming from the reader's perspective; (b), (e), and (h) to an along-strike source coming from inside the page; and (c), (f), and (i) correspond to the stacks of (a + b), (d + e), and (g + h), respectively. (a) to (c) are the radial components of the receiver functions (RFs) migrated without the scattering patterns and show coherent but relatively low amplitudes compared to Figure 5a. (d) to (f) are transverse and vertical components of the RFs migrated without the scattering patterns and show higher energy content but inconsistent polarities. In (g) to (i), the three components of the RFs migrated with the effects of the scattering patterns taken into account.

3.2. Scattering Patterns and Three-Component Migration

As shown in Cheng et al. (2016), the scattering patterns are important to account for amplitude variations and polarity reversals in the various phases. In this section, we illustrate this point by applying the method to the synthetic case WCS1 described in Table 1, with a single 40° dipping interface. Results are shown in Figures 5 and 6, where arrows and symbols indicate the direction of the propagation of the incoming waves. In each row of these figures, the images are normalized by the maximum absolute amplitude of the strongest image.

The migrated images for the *PS* mode of two sources located on opposite sides of the structure, both in the imaging plane, are shown in Figure 5. The wavefield for the first source (left column) comes from a downdip direction, which is to the right in this geometry. The wavefield for the second source (middle column) comes from an updip direction, which is to the left in this geometry. The results for two sources that were rotated 90° compared to the previous ones, which puts them in the strike parallel plane, are shown in Figure 6. The wavefield for the first source (left column) comes from the reader's perspective into the figure, and the wavefield for the second source (middle column) comes from the opposite direction, facing the reader. We illustrate our method with single-source migrations by introducing the various elements described in section 2 one by one. Table 2 describes which elements of the imaging principle are taken into account in every figure.

We shall now describe each panel of Figures 5 and 6. In Figure 5 we migrate the radial component of the *PS* mode in the simple 2-D model WCS1 to show the effect of applying the scattering pattern corrections. The images from Figures 5a to 5c (top row) are migrated without taking the scattering patterns into account. In Figure 5a (source on the right-hand side, first column) the migration algorithm focuses most of the energy on the discontinuity (dashed line). However, the free surface backscattered phases leak into the image and introduce spurious structures with higher dip values and alternating signs. In this migrated image, some of the scattered energy is also smeared above the discontinuity. The image in Figure 5b shows that for a source on the opposite side (second column), the migration also focuses the energy on the discontinuity at the correct depths, but the polarity reversal has not been accounted for, and the sign of the migrated scattering potential is negative. Notice also that this image contains slightly less energy from the multiples as this particular geometry generates less scattering overall on the radial component of the RF. Figure 5c shows that the image generated by linearly stacking over both sources (third column) is dominated by the wavefield coming from the downdip direction and that the two sources interfere destructively where they are supposed to stack up.

If we apply the amplitude and polarity corrections given by scattering patterns and redo the same migration, we can see on Figures 5d and 5e (bottom row) that the sign of the scattering potential of the imaged structures are now coherent for the two sources. We also note that the image based on a wavefield coming from the downdip direction (source on the right-hand side, first column) is significantly clearer as the positive and negative parts of the scattering pattern correction ellipse globally cancel out far away from the scattering interface. The results in Figure 5f show that this time the two images interfere coherently where they are expected to. This proves that taking scattering physics into account greatly improves the imaging: We migrate the correct polarities each time, and hence, the images stack constructively. We eliminate the polarity problem for large dip angles and can automatically assimilate data from all slownesses.

The benefit of migrating the three components of the RF for large dips and oblique, along-strike arrivals in the WCS1 scenario is shown in Figure 6. We show that there is much complementary information to be gained from three components migration, provided that polarity reversals are properly accounted for. Similarly to Figure 5, we migrate the *PS* mode for the same simple 2-D model. The results in Figures 6a to 6c (top row) show the migrated images of the radial component for two sources placed symmetrically on one side (into the page, first column) and the other (out of the page, second column) of the dipping structure. It shows identical images for the two sources, which is expected. The signs of the discontinuities are correct in both images for the *PS* mode, but we also observe considerable energy from the *PpS* and *PsS* multiples stacked on the left side of the images. The summed image (third column) in Figure 6c shows the same attributes. However, the maximum absolute amplitude in this image is lower than in Figure 5a. When migrating the transverse and vertical components of the RF in Figures 6d and 6e (middle row), the maximum amplitude is higher, but there are polarity issues. Moreover, the images are not identical anymore because the transverse component is defined in opposite directions for both sources. Therefore, we can see in Figure 6f that the stack of the two previous images does not give a satisfactory result. By applying the scattering patterns on the three components, we solve the problem in Figures 6g to 6i (bottom row). In this case, by migrating the three components of the RF with their proper scattering weights, we find identical images again, which is what we expect after the correction, and the amplitude in the stacked images are on the same order of magnitude as their counterparts in Figure 5. Additional tests for zero to very large (80°) dips are available in Figure S1 in the supporting information.

Further testing taking into account only the phase term, or polarity, of the scattered signals yielded degraded images in which the spurious features are enhanced. This is because such strategies place a high weight on ray configurations where no scattering is expected. In the tests that we ran, this happens to enhance especially the contaminating signals. These results show that taking the amplitude term of the scattering

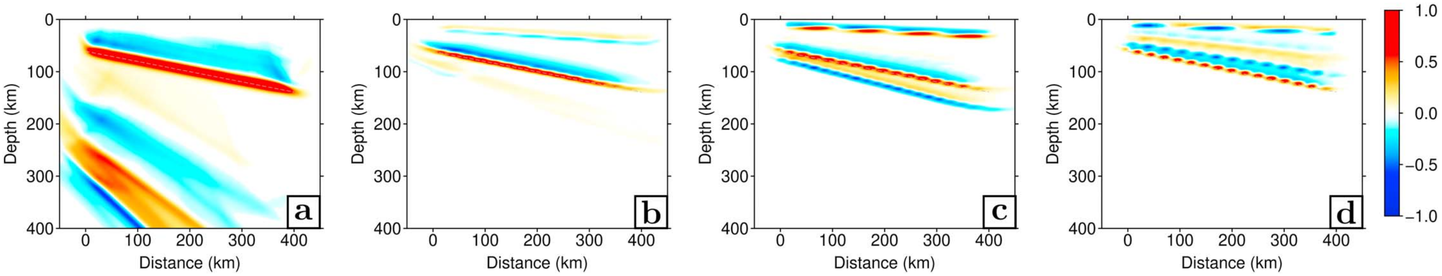

Figure 7. Single-mode migrations of three components receiver function for a 2-D model containing a single interface with 10° dip and 10% δV_P, δV_S, and $\delta\rho$ perturbations (Model WCS2; Table 1). Panel (a) is the *PS*, (b) the *PpP*, (c) the *PpS*, and (d) the *PsS* migrations (cf. text). The data were generated for 24 sources regularly spaced in back azimuth and with epicentral distances ranging between 30° and 90° . The four images recover the structure with the correct polarity but are affected by the other modes. The spurious migrated signals are at different locations in each migration.

patterns into account is key to reducing the contamination of migrated images by the various scattered modes.

Here we demonstrated the importance of the scattering patterns when migrating three component data. Moreover, we showed that integrating the three components of the RF into the imaging principle allows us to coherently retrieve the scattering potential for arbitrarily dipping discontinuities from all back azimuths.

3.3. Multimode Migration

As seen in Figures 5 and 6, free surface multiples are clearly visible in the *PS* migration, even for very simple settings. They are easily distinguishable in the *PS* migrated image for this particular model, but their interpretation becomes increasingly more difficult with the complexity of the setting. Here we will show how jointly migrating the four main scattering modes can help mitigate the contamination by free surface multiples in the interpretations of migrated images.

Since free surface multiples tend to be stronger and more difficult to interpret correctly in subhorizontal settings, we choose a model with a 10° dipping interface, thus placing ourselves in a worst-case scenario situation with regards to free surface multiples (Cheng et al., 2017). In this simulation we use 24 sources to cover all possible back azimuth and incidence angles. The results in Figure 7 show the migrations for the four individual scattering modes for model WCS2 described in Table 1, which has one interface at a 10° dip.

The results for the three-component *PS* migration are shown in Figure 7a. The dashed line shows the only feature that is present in the synthetic model. We can see a coherent signal that lines up with the structure, but also three spurious features associated with multiples: (1) a negative feature at approximately 180- to 380-km depth that corresponds to the *PpP* multiple; (2) a positive feature at 250- to 400-km depth that corresponds to the *PpS* multiple; and (3) a negative feature between 300- and 400-km depth that corresponds to the *PsS* multiple.

We perform one migration for each scattering mode, and the resulting images can be seen on Figures 7b (*PpP*), 7c (*PpS*), and 7d (*PsS*). We find that the free surface multiples in the synthetic waveforms are correctly migrated in their respective images. However, in each image, three out of the four modes are still visible and wrongly migrated. They appear at different depths and produce spurious structures with different dip angles. Specifically, phases slower than the currently migrated mode are mapped below the true scattering feature (e.g., in Figure 7a), and phases faster than the currently migrated mode are placed above the scattering feature (e.g., in Figure 7d). On these four migrated images, there is overall more spurious features than true features, but their locations are not coherent across the four single-scattering mode migrations. These four images allow us to visually discriminate between real features, which have coherent amplitude across all four images, and the spurious features, which do not correlate on the different single-scattering mode images.

In this example, we can also notice that the time delays are more compressed in the multiple modes, and hence, they have a higher spatial resolution than the direct *PS* conversion mode, especially for the *S* scattered waves (Rondenay, 2009). This is due to the fact that a ray covers a single unit distance (upgoing) between two consecutive points in depth for the *PS* mode and two (downgoing and upgoing) when we migrate a multiple.

Here we showed that we are able to migrate the free surface multiples at their correct polarities and positions in depths using the scattering patterns and their respective traveltimes computed with FM3D. Because the

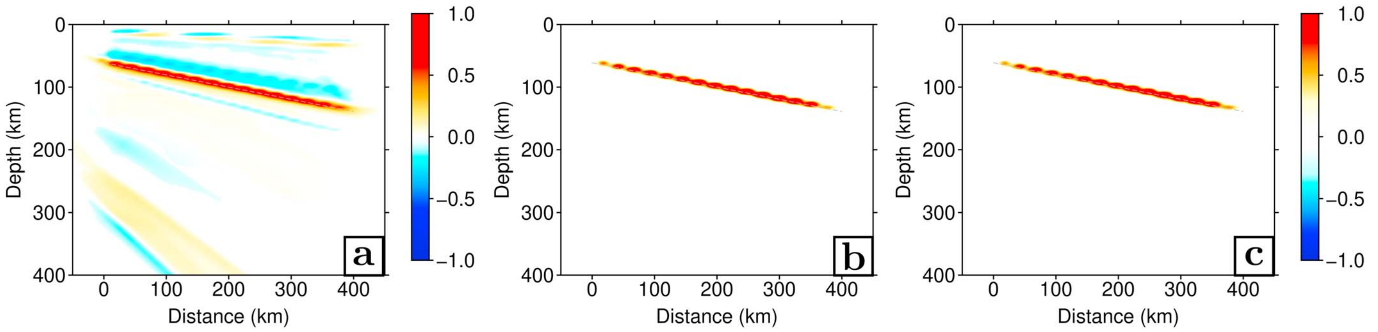

Figure 8. Multimode migrations for a 2-D model containing a single interface with a 10° dip and 10% δV_P, δV_S, and $\delta\rho$ perturbations (Model WCS2; Table 1). (a) Linear stack, (b) phase-weighted stack, and (c) second-root stacks for the multimode migration of the three-component receiver functions with scattering patterns, for 24 sources coming from all azimuths with epicentral distance between 30° and 90°.

actual features are always focused at the same depth across all single-scattering mode images, they will sum up positively during the multimode migration. This is something we will exploit in the next section.

3.4. Stacking Methods

We now test the three stacking methods introduced in section 2.7 to see how well they enhance the coherent signals from the four single-scattering mode migrated images in Figure 7. We consider one stacking method with no coherence filter (linear stacking; equation (13)) and two stacking methods that incorporate coherence filters—PWS (phase coherence filter; equation (16)) and second-root stacking (amplitude coherence filter; equation (19)). The results are displayed in Figure 8.

The first method we test is linear stacking (equation (13); Figure 8a), where we simply add the amplitudes of the four modes during the migration with no extra measure of coherence. The resulting amplitudes are then normalized to obtain the final image. Results show that the dipping interface is better imaged than in Figure 7a. We note that the energy from spurious features is considerably reduced but that they do not completely disappear. The three spurious streaks described in Figure 7a are still present just under the actual discontinuity. We also see that there is more noise above the discontinuity than in Figure 7a. In this case, the four modes have comparable amplitudes, and spurious features will only be reduced to about one fourth of their amplitude on a given scattering mode migration.

The second method we test is PWS and corresponds to the imaging principle in equation (16). The results are shown in Figure 8b. The resulting image exhibits fewer artifacts than with the linear stack, as most spurious signals do not have a coherent phase over the four modes. The phase stack virtually acts as a filter applied to the linear amplitude stack, as the artifacts are at the same position in depth, but their amplitude is even more reduced, representing less than 10% of their single-mode values.

Finally, the last method we test is second-root stacking and corresponds to the imaging principle in equation (19). The results are shown in Figure 8c. The image is very similar to Figure 8b and has all the artifacts reduced to less than 10% of the actual discontinuity.

The test conducted in this section demonstrate that most artifacts can be eliminated by applying coherence filters based either on phase (phase-weighted stack) or amplitude (second-root stack) in simple synthetic cases. We are now going to test these methods with a more complex synthetic model depicting an idealized subduction zone.

3.5. The 2.5-D Subduction Zone

Here we show how our imaging principle can be used to improve interpretations in realistic settings. To do so, we design a synthetic subduction zone model, labeled R2DSZ in Table 1, and analyze the migrated images obtained using equations (12), (13), (16), and (19). In this model, we have four different layers over a half-space with constant elastic properties and use a total of 24 sources equally spaced in back azimuth with random epicentral distance to the center of the array ranging between 30 and 90°. The array starts at lateral position 0 km and covers 400 km in length.

The results for the four single-mode migrations are shown in Figures 9a to 9d. Figure 9a shows the migration of the forward *PS* scattering mode. The single-mode migration is able to resolve the overriding Moho and the

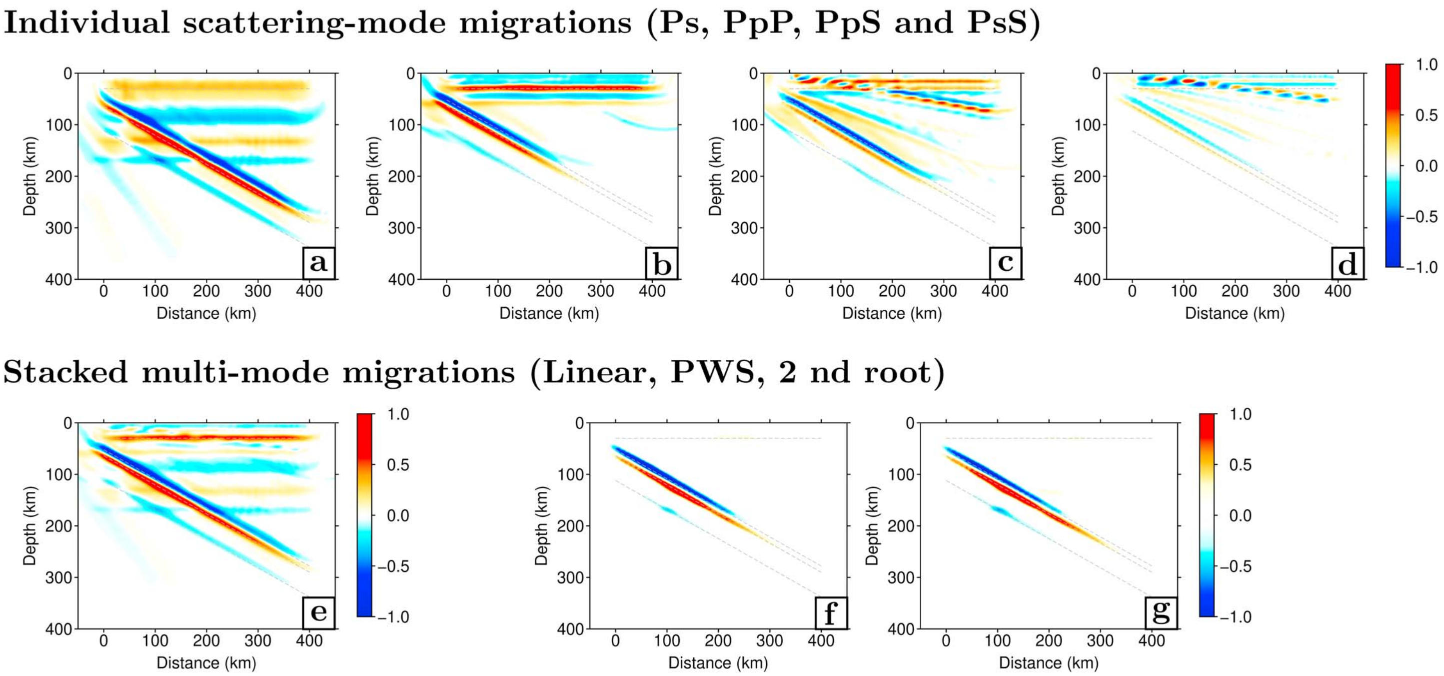

Figure 9. Single-scattering mode and multimode migrations for the 2.5-D subduction zone (Model R2DSZ; Table 1). The upper four images (a = *PS*, b = *PpP*, c = *PpS*, and d = *PsS*) are the four migrations for the four single-scattering modes (equation (13)). The lower three images correspond to the linear (e; equation (14)), phase-weighted (f; equation (16)) and second-root (g; equation (19)) stacked images. PWS = phase-weighted stacking.

various dipping interfaces belonging to the oceanic lithosphere, but there are strong artifacts in the migrated image. In the right part of the image, we observe that for a simple 30-km-deep Moho model, the free surface multiples can become predominant at around 100 km where one could interpret a spurious LAB. Figure 9b shows the backscattered *PpP* migration. The structure comes out more clearly because the *PpP* scattering mode is well isolated from the other phases—that is, it is polarized mostly along the vertical component, in contrast to *S* waves from the other scattering modes, which are polarized mostly along the horizontal components. The results in Figures 9c and 9d show the backscattered *PpS* and *PsS* migration, respectively. Figure 9c exhibits clearly defined structures corresponding to the Moho and the subducting slab. Figure 9d recovers the dipping interfaces well but shows only a very weak signal for the continental Moho. This is due to the resolution of the migration grid, which is too low (5 km vertically) to image the highly vertically compressed signal of the *PsS* mode at the Moho level for a 1-Hz synthetic RF. In addition, Figures 9c and 9d also display some strong artifacts in the overriding mantle wedge, which correspond to the spurious migration of other slab conversions. The higher resolution of the backscattered *S* modes is visible on these last two figures.

Overall, the four scattering modes produce a coherent view of the imaged medium. However, there are some notable differences between them. On one hand, the amplitudes of the shallow structures are stronger in images based on multiple modes than on those based on the direct mode. This can clearly be seen by comparing the *PS* and *PpP* images. On the other hand, the images based on multiple modes have less imaging power in the lower part of the image because phases reflected on the top of dipping interfaces at these depths are not recorded on the array and leave the imaged region. In each of these single-mode images, the specific scattering mode that is being processed is always migrated at the correct position, while the other modes are migrated as spurious features at different locations. Finally, we note that the signal of a discontinuity in a given mode can be affected by destructive interference with the projected signal from another discontinuity in another mode. This is best exemplified in the *PpS* and *PsS* images, where destructive interference between the continental Moho signal and the *PS* scattering from the subducting slab generates an apparent hole in the continental Moho even if it is a continuous feature.

The results for the three different stacking methods are displayed in Figures 9e to 9g. Figure 9e corresponds to the linear stack. It represents a considerable improvement over Figure 9a, especially for the shallow structures. However, because the *PS* mode is dominating the final image, phases reflected at the continental

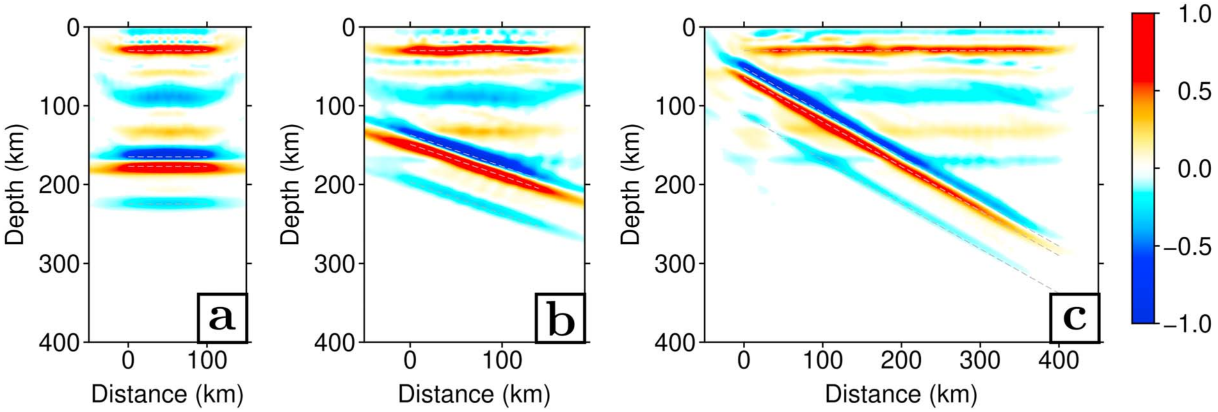

Figure 10. Off-dip profiles across the 3-D-migrated image of Model R2DSZ. The imaging principle is the same as the linear multimode as in Figure 9e (equation (14)). The receiver array is 100 km in the along-strike direction and 400 km in the dip direction. Profiles are cut through the imaged volume at azimuths of (a) 60°, along-strike; (b) 105°, oblique; and (c) 150°, dip. The imaging principle recovers the correct depths and dips of structures in all cases, regardless of orientation. Some artifacts can be seen in (b) and (c) at the continental Moho because of the interference with the *PpP* and *PpS* scattering modes from the dipping interfaces.

Moho and migrated as *PS* transmissions are still visible. We also note that the contamination from free surface multiples for the dipping interfaces is strongly reduced. Figure 9f corresponds to the phase-weighted stack, which focuses the energy even more at the true location of discontinuities in the subducting slab. However, we note that the Moho is no longer visible. This is because the Moho is absent from the *PsS* migration, which leads to incoherent signals across the scattering modes, and subsequent down-weighting in the nonlinear stack. Nonetheless, there are no more visible artifacts in the rest of the image. Finally Figure 9g corresponds to the second-root stack. This image is very similar to the phase-weighted migration, and the slab is recovered down to more than 200-km depth.

The results in Figure 9 prove that it is necessary to adopt a multimode migration strategy in order to avoid misinterpreting Moho multiples as a potential LAB. We also note here that the best imaged dipping interface is the subducting Moho, which corresponds to a 24% jump in seismic velocities. The top and bottom of the dipping slab correspond to 19% and 6% jump in seismic velocities, respectively, and are clearly visible in the *Ps*, *PpP*, and *PpS* individual scattering modes and in the linear stack images. Conversely, the continental Moho suffers from the limited vertical resolution of this test setting. Being almost absent in the *PsS* migration, it is completely removed from the nonlinear stacks. This can be mitigated by improving the vertical resolution of the migration grid at the expense of computation time.

Though our models are not truly 3-D, we can still test the 3-D capabilities of our method by investigating how it recovers structures for profiles that are not aligned with the dip direction. Methods that are purely 2-D, such as the GRT and RTM, cannot recover the structure at oblique angles, because it effectively becomes a 3-D problem (see, e.g., Rondenay et al., 2010). Figure 10 shows a series of profiles cut at various azimuths through our 3-D image of R2DSZ. We find that the off-dip profiles recover the slab structure as well as the dip profile, confirming that our approach can handle 3-D geometries and that the recovered migration model is fully 3-D.

The results from this section show that the imaging principles that we developed in section 2 are able to structure in both challenging and realistic settings provided that the vertical resolution is high enough. We tested the method with worst-case scenarios with respect to polarity artifacts (WCS1) and strong free surface multiples (WCS2), as well as with a synthetic 2-D subduction zone (R2DSZ). The data can be automatically processed with the scattering patterns on three components, and the recovered model is fully 3-D. This ensures maximum data coverage and allows for good focusing of the migrated energy along the scattering interfaces.

4. Application to Field Data and Implications

We now apply the imaging principles to field data from the Multidisciplinary Experiments for Dynamic Understanding of Subduction under the Aegean Sea (MEDUSA) array in the Hellenic subduction zone

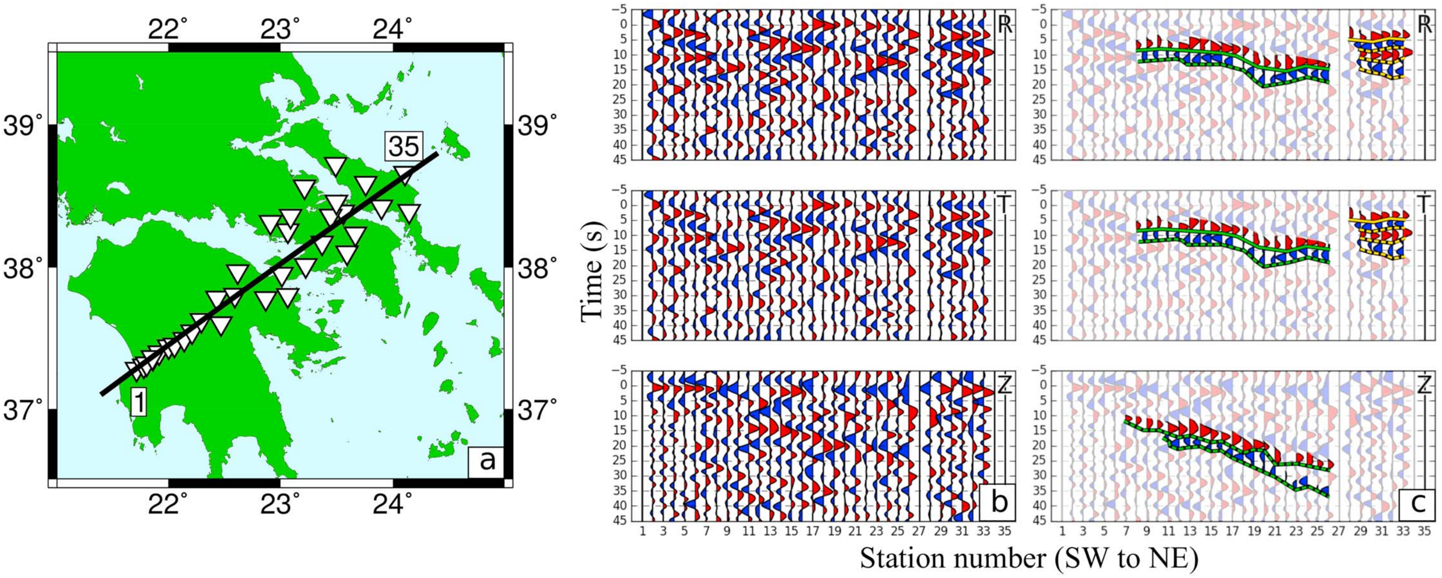

Figure 11. Setup, raw, and interpreted date from the Multidisciplinary Experiments for Dynamic Understanding of Subduction under the Aegean Sea experiment (Pearce et al., 2012). (a) corresponds to the array setup, with white triangles representing the stations position from 1 (southwestern corner) to 35 (northeastern corner) and the projecting line in solid black. (b) is the data for one event sorted by station number. (c) is the interpreted data where we highlight the presence of the continental Moho (orange) and the subducting slab (green). We differentiate between the forward conversions (solid lines) from the free surface multiples (dashed lines).

(Rondenay, 2006). We will show that our method can retrieve the subsurface structure with fine details. Here we use a 1-D reference velocity model, even though our method is capable of handling a 3-D model, because we want to replicate the GRT images from Pearce et al. (2012), which were obtained with the same data set.

4.1. Hellenic Field Data

The Hellenic subduction system represents an ideal laboratory to investigate the complex mechanisms that control oceanic and continental subduction. It spans 1,300 km from the southeastern tip of Puglia in Italy to the region of Antalya in Turkey and has a convergence rate of 4 mm/year. In this work, we aim to investigate the structure of the subducting slab in the Western Hellenic Subduction Zone (WHSZ). This is the part of the subduction system that surrounds mainland Greece and the Peloponnese region from the West before transitioning into the Southern Hellenic Subduction Zone offshore Crete.

Both oceanic and continental subduction coexist in the WHSZ, and the link between the two systems has only been partially explained so far. Previous studies have shown that the convergence rates and slab retreat behavior strongly depend on the slab composition (Papanikolaou & Royden, 2007). The slab composition and water content also influence the hydration of the mantle wedge and the volcanic activity in the region, which have been studied structurally and geochemically (Pe-Piper & Piper, 2007). Complementary geophysical methods such as long-period magnetotellurics have found potential fluid pathways, emerging both from the upper part of the slab and deeper portions of the subduction (Galanopoulos et al., 2005; Tzanis et al., 2018).

The data that we use in this application comes from the MEDUSA project, which was carried out across the WHSZ (Pearce et al., 2012). This experiment had two seismic lines deployed. The first line was in the northern part of the region, spanning roughly from Corfu to Thessaloniki, and was aimed at studying the continental subduction. The second line was deployed in the southern part of the region and targeted the oceanic subduction under the Peloponnese and across the gulf of Corinth. Here, we take the data from the southern line to test our imaging principle. The data along this line are of higher quality than the northern line, and the images display clearer features (Pearce et al., 2012). The station distribution is shown in Figure 11a.

The direct and scattered wavefields are estimated using a multichannel approach on the 3-D *P* wave as described in section 2. The data set consists of 52 events recorded at 35 temporary stations over the course of 1.5 years, with a total of about 1,500 waveforms available. The maximum frequency of the data is 0.5 hz.

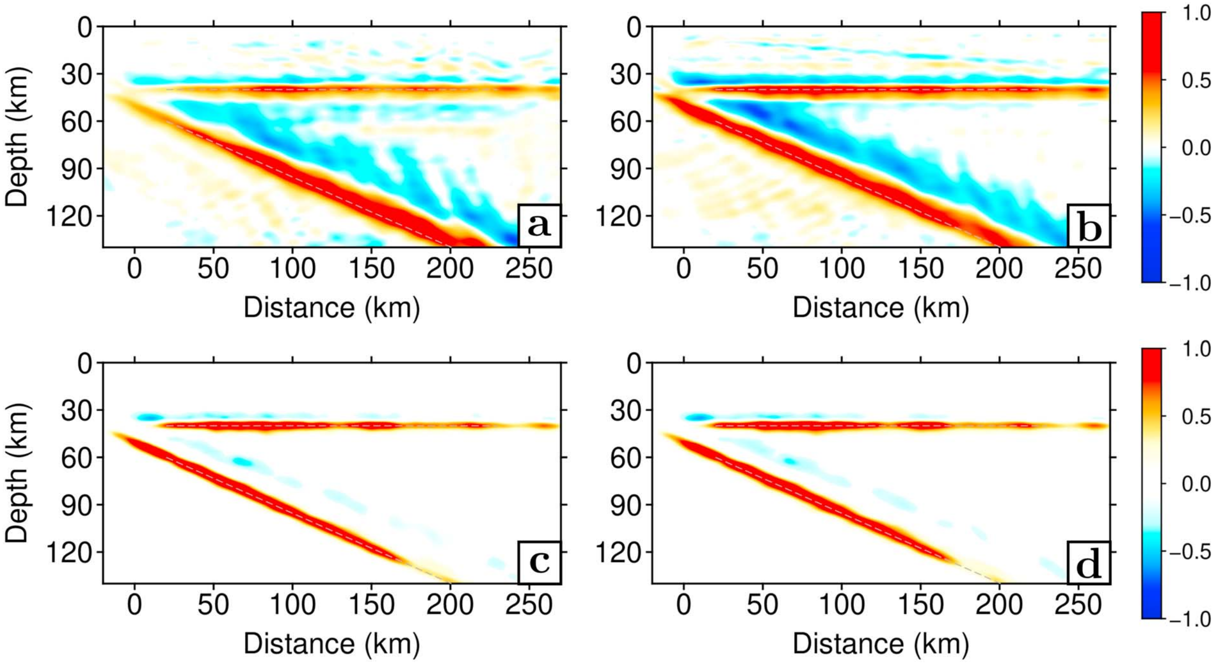

Figure 12. Resolution test with a three-layer synthetic model for the geometry source distribution of the Multidisciplinary Experiments for Dynamic Understanding of Subduction under the Aegean Sea experiment. Panel (a) shows the linear multimode migration with original station geometry. Panels (b)–(d) are the linear, phase-weighted, and second-root multimode stacks with data projected on the migration line, respectively (i.e., equations (14), (16), and (19); see text).

The data are selected on an event-by-event basis based on visual inspection of single-event migration results. We analyze the 52 single-event images and reject data in two cases. First, we reject events when the migrated images display only horizontal streaks with a single main frequency. In the data space, this corresponds to traces dominated by unwanted oscillations, most likely linked to the deconvolution. Second, we reject events when the migrated images are dominated by southward dipping discontinuities, as it is the opposite behavior to northward dipping subduction that we are imaging. Based on this selection scheme, we retained 32 high-quality events for the final migration.

In their paper, Pearce et al. (2012) migrated the data using a GRT method that shares some similarities with our method but is limited to 2-D geometries (Bostock et al., 2001). Using data from their study, we have reproduced the single-scattering and multimode GRT images of Pearce et al. (2012). They are shown in Figure S2. The multimode image shows a clear Moho in the overriding plate, as a continuous interface that smoothly dips southwestward from 30- to 40-km depth. It also shows clear signals from both the upper and lower limits of the subducting crust, which dips northeastward at 17° down to about 100-km depth. In order to better compare our 3-D images to previously published 2-D results, we alter the original station distribution by projecting their location on the migration line used by Pearce et al. (2012). Note that there is an equivalent step in the GRT preprocessing (Rondenay et al., 2001).

Raw and interpreted data from a single event, filtered at 0.1 Hz, are displayed in Figures 11b and 11c. In the northeastern (stations 28 to 35) part of the section, we observe signals corresponding to the overriding Moho and its free-surface multiples on the radial and transverse components at around 3- to 15-s delay. The PS conversion from the slab is visible at 5- to 10-s delay on the radial component. Strong signals from multiples on the vertical component are visible at 10- to 30-s delay on Stations 2 to 26.

4.2. Resolution Test

In order to determine how well our method will be able to perform with this data set, we first perform a synthetic resolution test on a 2-D subduction model. We generate data for all 52 events recorded at a 35 stations setup corresponding to the MEDUSA south line. The results will be used to determine the maximum resolution we can achieve given the data coverage, maximum frequency, and station distribution. In order to better compare our image with GRT or RTM migrations, we project the locations of stations on the imaging line as previously stated.

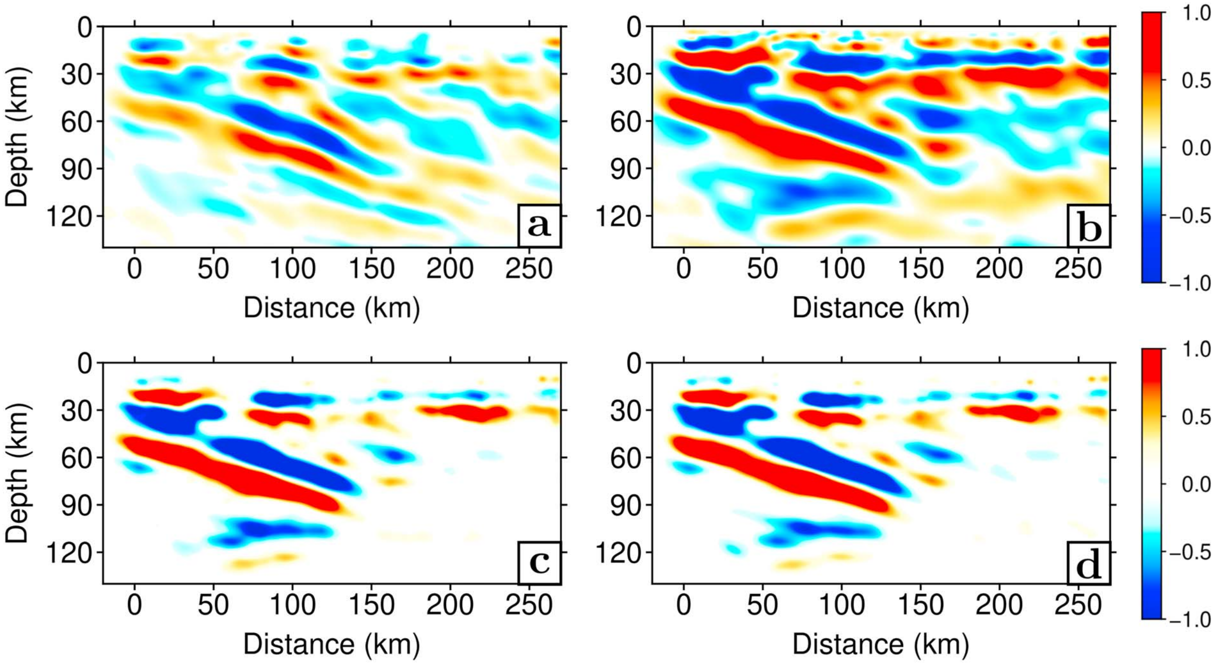

Figure 13. Images obtained with the multimode migration on the Multidisciplinary Experiments for Dynamic Understanding of Subduction under the Aegean Sea experiment data set (Pearce et al., 2012). Panel (a) shows the linear multimode migration with original geometry. Panels (b)–(d) show the linear, phase-weighted, and second-root multimode stacks with data projected on the migration line, respectively (i.e., equations (14), (16), and (19); see text). The overriding Moho, the subducting crust upper and lower limits are clearly imaged.

To perform this test, we design a three-layer reference model described in Table 1 as MRT. The first layer is the 40-km-thick overriding crust, then there is a 10% velocity increase at the Moho and another 10% velocity increase at the slab interface. Since the amplitude of the velocity jump is similar for the two interfaces, we expect the two interfaces to show the same scattering potential on the final image. The data are generated with the Raysum code and has a dominant frequency of 0.3 Hz. This corresponds to wavelengths up to 20 km for *P* waves and 10 km for *S* waves, so for the resolution test and the real data we use a $2 \times 2 \times 2$ km voxel size. Because the backscattered *S* wave multiples have shorter wavelengths in the model space, we allow for the data to be migrated in different frequency bands for the various scattering (see, e.g., Tauzin et al., 2016).With an average station spacing of just under 10 km, a 40-km-deep Moho should be easily retrievable.

Results for this synthetic resolution tests (with same frequency range for all modes) are presented in Figure 12. Figure 12a shows the result for the fully 3-D imaging principle in equation (13), without projecting the stations on the migration line. The energy focuses on the discontinuities, but there are some small coherent artifacts under the Moho with both negative (55-km depth) and positive (65-km depth) energy values. The features are retrieved at their correct positions, but there are along-profile heterogeneities introduced by the uneven spatial distribution of stations. We individually down-weight the stations that are closer together in an effort to normalize the energy content across the image.

Figure 12b shows the result for the linear multimode stack with the array projected on the migration line and with individual station weights. The discontinuities are highlighted more finely with less along-dip variations. Nevertheless, some artifacts still remain, especially around the overriding Moho. Figure 12c shows the result for the phase-weighted stack from equation (16) with station weights and station projection. There are fewer artifacts around the Moho than with the linear stacking. Figure 12d shows the result for the second-root stacking with the individual station weights and station projection. Here also, there are practically no artifacts left in the vicinity of both the overriding Moho and the subducted slab.

This synthetic example shows that our method is capable of retrieving subsurface structure from an experimental setup such as that afforded by MEDUSA. The three stacking methods produce robust results and are efficient at removing most of the spurious energy from the final image. We expect to retrieve both flat and dipping discontinuities in the data and are confident that we can recover the structure properly in the field data using the multimode algorithm.

4.3. Field Data Migrated Sections

The migrated sections for the MEDUSA data are presented in Figure 13 (see Figure S2 for the single mode unstacked images). The background velocity model for the migration is the same 1-D model as that used by Pearce et al. (2012) and is described in Table 1 as MPKDM. We apply the following treatment to the data to enhance the imaging quality. We filter the data in different frequency bands to account for the difference in resolution power between the four modes (Tauzin et al., 2016). This helps to maximize the coherence on the final images. We filter the data between 0.03 and 0.5 Hz for the PS and PpP data and between 0.03 and 0.3 Hz for the *PpS* and *PsS* data. As we showed in the resolution test, we obtain the best images when we apply a weight that takes into account interstation spacing. Therefore, we down-weight the data from the stations that are closer together to homogenize the energy content on the cross-section in Figures 13b to 13d.

The results obtained with the different stacking methods are comparable overall with previous results from, for example, Pearce et al. (2012). Two main features can be observed in the migrated sections: (1) a 25- to 35-km-deep (from NE to SW) overriding Moho and (2) a 12-km-thick, 18° northeastward dipping subducted crust. The Moho signal disappears close to the slab interface, whereas the subducting crust signal disappears at 85 km for the upper limit and 100 km for the lower limit. The strong similarities between our images and those of Pearce et al. (2012) can be attributed, at least in part, to the fact that the two methods share exactly the same preprocessing steps. This results in identical geometrical setups and data sets prior to filtering and application of the wavelet shaping factor.

We shall now describe each image individually, starting with Figure 13a. The first image shows the linear multimode stack for the initial fully 3-D geometry, similar to Figure 12a. Here the overriding Moho and the subducting crust are visible, but the image is noisy. Next, Figure 13b shows the result for the linear stack with data that has been projected on the migration line and with the individual station weights, similar to Figure 12b. In this case the overriding Moho clearly appears as a linear feature, and much of the noise has disappeared. The slab signature is also more consistent than on Figure 13a, with a constant thickness. We can see a gap in the overriding Moho very close to where it intersects the dipping slab. This gap can be partially explained by the interference between the signals from the overriding Moho and the top of the slab in different migration modes, as stated in section 3.5. Lastly, Figures 13c and 13d show the results for the phase-weighted stack and second-root stack, respectively. Colors have been saturated to emphasize the coherent structure. The two images are very similar. The signature of the overriding Moho is intermittent across these profiles. At greater depth, the bottom and top of the subducting crust are clearly isolated from their surroundings, and there is less noise in the slab. The dipping signal is probably lost at depth due to eclogitization, as explained by Pearce et al. (2012). We acknowledge that we cannot interpret amplitudes in terms of velocity contrast $\delta\beta/\beta$ in the images generated by our method. However, we find that the three main discontinuities, namely, the top of the subducting crust, the slab Moho, and the overriding Moho, have approximately the same scattering potential in our images. This roughly translates into the same changes in elastic properties, which is consistent with the previous GRT images (Pearce et al., 2012).

5. Discussion: Advantages and Drawbacks of the Method

In this paper, we presented a new, fully 3-D prestack migration method and demonstrated its applicability through a set of synthetic examples and a field case study. Here we will shortly discuss the advantages and drawbacks of our method compared to other imaging approaches based on scattered teleseismic waves.

5.1. Scattering Potential Versus Elastic Perturbations

Our method projects and stacks teleseismic waveform data in the depth domain to recover scattering structure. Other methods have the same basic principle, ranging from fast 1-D CCP stacking (Dueker & Sheehan, 1997) to 2-D multimode CCP (Tauzin et al., 2016) and 3-D prestack techniques (this paper; Hansen & Schmandt, 2017). All these methods afford very high spatial resolution corresponding to one wavelength λ for *PS* scattering and $\lambda/2$ for multiple modes, and prestack techniques are able to image structures as shallow as two times the interstation spacing down to approximately the same depth as the array aperture (Miller et al., 1987; Rondenay, 2009). These methods have high spatial resolution, but all suffer from the fact that they provide information only about the location of the scatterers, not about their elastic perturbations.

In order to obtain high-resolution elastic parameter perturbations, some authors combined prestack imaging methods, which have high spatial resolution, and inversion schemes that allow to distinguish density from velocity and access elastic parameters perturbations. Methods like the GRT migration (e.g., Bostock et al.,

2001) recover these perturbations across scattering interfaces using linearized inversion techniques. Other methods like RTM rely on wavefield reconstruction across the whole study area for both the upgoing and reflected scattering modes. This requires accurate and expensive interpolation of the data into the model. The drawback with these methods is that they are computationally expensive and that the inversion steps require dense data coverage on all arrival geometries—that is, comprehensive ray coverage over a slowness hemicircle in 2-D and a slowness × back azimuth hemisphere in 3-D. These two factors limit these methods mostly to 2-D applications, while our method allows us to move to 3-D migration.

Migration methods such as ours can be complemented by pure inversion approaches, which use the data to create a model parameterized in terms of elastic perturbations and go beyond the stacking offered in classic migration. Scattered waveforms can be used in expensive full waveform inversion schemes where the wave equation is solved in 3-D (*P* wave coda waveform inversion; Frederiksen & Revenaugh, 2004). However, these are very expensive and do not provide the high-resolution power of migration methods, as they are often mixed-determined problems that require regularization, which reduces their resolution power. Another way to use the scattered data is in joint inversions with surface waves and other body waves (e.g., Bodin et al., 2016) using a fully nonlinear Bayesian inference. This allows to estimate precise uncertainties about the elastic and structural parameter variations, but extensive model sampling has limited its application to 1-D structure so far.

5.2. Three-Dimensional Seismic Imaging

In order to obtain high signal-to-noise ratio and interpret scattered data, migration methods require a large number of waveforms to be stacked. In CCP stacking, the waveforms are first stacked according to their incoming geometry and then projected in the depth domain, which effectively collapses the 3-D data on a horizontally layered 1-D profile. Including lateral variation effects back in the waveform stacking can be partially addressed by performing wave number filtering or designing 2-D migration schemes (Bostock et al., 2001; Burdick et al., 2013; Chen et al., 2005; Tauzin et al., 2016). Three-dimensional elastic parameter variations can be treated to first order by computing the arrival times or full waveforms in a 3-D reference model. However, there will always be some contamination if there are large lateral variations in structure or elastic properties.

Our method is a 3-D prestack migration, which works in the opposite way to CCP stacking. In our case, projecting the data independently before the final stacking allows to preserve the 3-D effects and thus avoids to make any assumption about the scattering structure that we want to image. In this way, our method exhibits close to no artifacts when dealing with dipping interfaces and laterally varying media and thus performs generally better than classic CCP stacking (Cheng et al., 2016). The drawback is that not using the horizontal interface assumption to stack all the traces slows down the depth mapping of the scattering information (Dueker & Sheehan, 1997). In this regard our method is very close to GRT migration. However, the dense data coverage required in GRT to perform a stable and meaningful inversion of elastic parameters is no required here as we simply migrate the scattering potential. This allows our method to be correctly applied in 3-D even without optimal data coverage.

Adapting Kirchhoff migration into migration and inversion schemes for passive seismology has been pioneered and improved in the last 20 years (Levander et al., 2005; Ryberg & Weber, 2000; Sheehan et al., 2000; Wilson & Aster, 2005). However, none of those methods have attempted fully 3-D migration, as computation time has always been a hurdle. Wilson and Aster (2005), for example, computed the arrival times in a one 1-D reference velocity model to speed up computations. The final step toward fully 3-D migration was taken by introducing 3-D wavefront calculation (Cheng et al., 2016), but this method was only very recently extended to fully 3-D by applying the fully 3-D scattering patterns (this paper; Hansen & Schmandt, 2017). In our implementation of the Kirchhoff imaging principle, by computing the arrival times with a fully 3-D scheme, we do not hinder our capacity to tackle even the strongest 3-D effects. This is done at the expense of some computational efficiency, but the overall cost is reduced by the introduction of the fast-marching method (FM3D; de Kool et al., 2006).

5.3. Scattering Patterns

CCP analysis uses only a small part of the scattered wavefield, usually either the radial or the Q component of the RF, as they are the only components that are sensitive to scattering under the horizontal interface assumption. This usually produces good first-order images. However, in the case of dipping discontinuities, a lot more information about subsurface structure may be gained from multiple component analysis

(Tonegawa et al., 2008). Our method uses three-component RFs, similarly to inversion methods that use this multicomponent data RFs to reconstruct the 2-D or 3-D wavefield and elastic perturbations. However, one has to be especially careful about the polarity issues that come with scattering on dipping discontinuities.

Taking the physics of scattering into account to deal with the polarity issues is what allows this step-up in imaging quality. For waveform inversion methods this is done by solving the wave equation in 3-D, which is expensive. In our method, this is done through the use of scattering patterns. We separate the calculation of the phase (traveltimes), which we obtain by running the FM3D software, from the calculation of the amplitudes, estimated using precise scattering geometry and scattering patterns, to avoid having to solve the wave equation in 3-D. This way of computing scattering intensities is similar to what is done in GRT and is faster than full-wavefield computations used in RTM methods. Also, by using fully 3-D scattering patterns, as opposed to their projection in 2-D, we can treat all scattered phases, including S_V-to-S_V and S_H-to-S_H scattering.

As shown in section 2, the use of scattering patterns allows us to automatically process data from all slownesses and back azimuth without worrying about polarity and amplitude issues. Methods that do not take scattering patterns into account, such as CCP stacking and 1-D inversions, have to carefully select data to avoid these issues. This results in more data rejection and thus lower data coverage.

5.4. Multimode and Stacking Schemes

Other authors have implemented approaches that migrate multiple modes of teleseismic scattering (Bostock et al., 2001; Tauzin et al., 2016; Wilson & Aster, 2005). As shown in section 3, taking not only the *PS* mode into account but also the *PpP*, *PpS*, and *PsS* modes largely improves the imaging quality. In addition to enhancing the data coverage with new ray paths, extracting the information from individual modes and comparing images across modes allows to discriminate between real and spurious structures. We demonstrated, for example, that multimode migration is a powerful tool to avoid misinterpreting a spurious LAB. Multimode algorithms have been devised for numerous migration methods and consistently show clear improvements both in synthetic and field data applications (see, e.g., Tauzin et al., 2017).

One of the drawback in using the multiples in the migration scheme is the additional time required to migrate these data. In practice, however, many of the calculations for a given scattering mode can be used in the other modes. In our case, we use four different modes and three independent stacking methods, but the migration only takes about twice as long as the *PS* migration alone.

Combining the information extracted from all the scattering modes by stacking the images linearly is an efficient tool to extract coherent information (Bostock et al., 2001; Hansen & Schmandt, 2017). In the case of GRT, the *PS*, *PpS*, and *PsS* modes are combined to create a composite result for $\delta\beta/\beta$ variations, and the *PpP* mode gives the result for the $\delta\alpha/\alpha$ variations. In our case, as we cannot easily extrapolate the results to elastic parameter variations, we stack all four modes together to get a single final image (Figures 8a, 9e, 11a, 11b, 12a, and 12b). Our examples confirm that linear stacking of scattering potential offers a significant advantage over PS migration alone, as the resolution power for the multiples is higher and the combination of α and β variations helps clearly underline the structures.

Going past linear stacking, we explored a number of nonlinear stacking strategies for multimode data, as originally proposed by Tauzin et al. (2017) for multimode CCP imaging. We first implemented a phase-weighted stack where the complex phase of our RF signals is first migrated independently from the amplitudes and then applied as a coherence filter to the amplitude image. This generates a joint coherence map of all the modes that removes the spurious signals and enhances the coherent scattering. Then we implement a second-root stack where square-root amplitudes for all modes are migrated together before taking the whole stacked field to the power of 2. This allows smaller coherent scattering signal to reach higher amplitudes on the final migrated image while also efficiently removing the larger incoherent peaks across all modes. We proved that both stacking methods are very efficient at removing incoherent features across modes and that even though they act on a fundamentally different level, they have very similar stacking capabilities. They allow to nearly completely reject information that is present on only one mode, and maximum stacking is reached for features that are coherent on at least three modes.

5.5. Towards Fully 3-D Settings

Our application to field data consists of a 1-D array and a 2-D slice; therefore, it does not showcase the benefit of our fully 3-D approach. We acknowledge here that the full potential of our method in 3-D is yet to be demonstrated. However, there are two encouraging points that validate the potential of our method. First, we show that when performing the same processing to the data as for 2-D GRT, we get a similar image with our fully 3-D imaging principle. This demonstrates that our method is a minima as powerful as the GRT migration to image the underlying structure of subduction zones in terms of scattering potential. Second, we show in Figures 12a and 13a that by using the original station distribution, which deviates slightly from a 1-D array, we can still recover the main features observed by authors of previous studies in the region.

6. Conclusions

In this study, we designed a new method to migrate teleseismic RFs and recover the three-dimensional distribution of scattering structure in the subsurface. In order to overcome the drawbacks of both fast CCP methods (which rely on the assumption that the underlying discontinuities are horizontal) and complex RTM or GRT migrations (which are too computationally expensive to be run in fully 3-D settings), we designed a new, computationally efficient and fully 3D multimode Kirchhoff migration approach.

We adapted the Kirchhoff method from reflection to transmission scattering and applied it to passive seismic data. We expanded the work done by Cheng et al. (2016) to include three component data and free-surface multiples into an efficient multimode migration by computing the traveltimes for all scattered phases using the FM3D software. We use three-component RFs, 3-D scattering patterns, and coherence filters to extract the information from the data.

Our method was tested in challenging and realistic synthetic scenarios, using the Raysum package. It recovers scattering structures with minimal artifacts in all tested cases and allows to take lateral heterogeneities into account with reasonable computational time. Our fully 3-D method has a similar cost to 2-D GRT.

Using data from the MEDUSA experiment in the Hellenic subduction zone, we show that our method performs correctly on field data as well. The images we obtain are similar to the ones obtained with a 2-D GRT migration and serve as a benchmark for our imaging method. We believe that the passive multimode 3-D Kirchhoff migration method will prove useful in complex settings where lateral variations play a large role.

Acknowledgments
We want to thank Jean Virieux and Benoit Tauzin for helpful discussion about the methodological developments and Hellenic Subduction Zone image interpretation, respectively. We also thank two anonymous reviewers and the associate editor for their comments, which helped improve and clarify the manuscript. This work was funded by the European Unions Horizon 2020 research and innovation program under Grant Agreement 716542 and by the Research Council of Norway via the project Subduction zone Water and Metamorphism: A Modelling and Imaging Study (Project 231354). All data can be found on the Incorporated Research Institutions for Seismology (IRIS) Data Management Center and at https://doi.pangaea.de/10.1594/PANGAEA.901308 for the deconvolved receiver functions used in this study.

References

Abers, G. A., MacKenzie, L. S., Rondenay, S., Zhang, Z., Wech, A. G., & Creager, K. C. (2009). Imaging the source region of Cascadia tremor and intermediate-depth earthquakes. *Geology*, *37*, 1119–1122.

Beylkin, G., & Burridge, R. (1990). Linearized inverse scattering problems in acoustics and elasticity. *Wave Motion*, *12*, 15–52.

Bodin, T., Leiva, J., Romanowicz, B., Maupin, V., & Yuan, H. (2016). Imaging anisotropic layering with Bayesian inversion of multiple data types. *Geophysical Journal International*, *206*, 605–629.

Bostock, M. G., & Rondenay, S. (1999). Migration of scattered teleseismic body waves. *Geophysical Journal International*, *137*, 732–746.

Bostock, M. G., Rondenay, S., & Shragge, J. (2001). Multiparameter two-dimensional inversion of scattered teleseismic body waves: 1. Theory for oblique incidence. *Journal of Geophysical Research*, *106*, 30,771–30,782.

Burdick, S., de Hoop, M. V., Wang, S., & van der Hilst, R. D. (2013). Reverse-time migration-based reflection tomography using teleseismic free surface multiples. *Geophysical Journal International*, *196*, 996–1017.

Chen, C.-W., Miller, D. E., Djikpesse, H. A., Haldorsen, J. B. U., & Rondenay, S. (2010). Array-conditioned deconvolution of multiple-component teleseismic recordings. *Geophysical Journal International*, *182*, 967–976.

Chen, L., Wen, L., & tianyu Zheng (2005). A wave equation migration method for receiver function imaging: 1. Theory. *Journal of Geophysical Research*, *110*, B11309. https://doi.org/10.1029/2005JB003665

Cheng, C., Bodin, T., & Allen, R. M. (2016). Three-dimensional pre-stack depth migration of receiver functions with the fast marching method: A kirchhoff approach. *Geophysical Journal International*, *205*, 819–829.

Cheng, C., Bodin, T., Tauzin, B., & Allen, R. M. (2017). Cascadia subduction slab heterogeneity revealed by three-dimensional receiver function Kirchhoff migration. *Geophysical Research Letters*, *44*, 694–701. https://doi.org/10.1002/2016GL072142

Claerbout, J. F. (1985). Imaging the Earth's interior.

Cooper, G. R. J. (2009). Stacking phase coherent signals.

Costa, J. C., Medeiros, W. E., Schimmel, M., Santana, F. L., & Schleicher, J. (2018). Reverse time migration using phase cross-correlation. *Geophysics*, *83*, 1–65.

Cottaar, S., & Deuss, A. (2016). Large-scale mantle discontinuity topography beneath Europe: Signature of akimotoite in subducting slabs. *Journal of Geophysical Research: Solid Earth*, *121*, 279–292. https://doi.org/10.1002/2015JB012452

de Kool, M., Rawlinson, N., & Sambridge, M. (2006). A practical grid-based method for tracking multiple refraction and reflection phases in three-dimensional heterogeneous media. *Geophysical Journal International*, *167*, 253–270.

Dueker, K. G., & Sheehan, A. F. (1997). Manlte discontinuity structure from midpoint stacks of converted p to s waves across the yellowstone hotspot track. *Journal of Geophysical Research*, *102*, 8313–8327.

Frederiksen, A. W., & Bostock, M. G. (2000). Modelling teleseismic waves in dipping anisotropic structures. *Geophysical Journal International*, *141*, 401–420.

Frederiksen, A. W., & Revenaugh, J. (2004). Lithospheric imaging via teleseismic scattering tomography. *Geophysical Journal International*, *159*, 978–990.

Galanopoulos, D., Sakkas, V., Kosmatos, D., & Lagios, E. (2005). Geoelectric investigation of the Hellenic subduction zone using long period magnetotelluric data. *Tectonophysics*, *409*, 73–84. https://doi.org/10.1016/j.tecto.2005.08.010

Hansen, M. S., & Schmandt, B. (2017). P and S wave receiver function imaging of subduction with scattering kernels. *Geochemistry, Geophysics, Geosystems*, *18*, 4487–4502. https://doi.org/10.1002/2017GC007120

Langston, C. A. (1979). Structure under mount rainier, washington, inferred from teleseismic body waves. *Journal of Geophysical Research*, *84*, 4749–4762.

Lekić, V., & Fischer, K. M. (2013). Contrasting lithospheric signatures across the western United States revealed by SP receiver functions. *Earth and Planetary Science Letters*, 1–13.

Levander, A., & Miller, M. S. (2012). Evolutionary aspects of lithosphere discontinuity structure in the western U.S. *Geochemistry, Geophysics, Geosystems*, *13*, Q0AK07. https://doi.org/10.1029/2012GC004056

Levander, A., Niu, F., & Symes, W. W. (2005). Imaging teleseismic P to S scattered waves using the Kirchhoff integral. *AGU Monographs*, 1–13. https://doi.org/10.1029/157gm10

Liu, K., & Levander, A. (2013). Three-dimensional Kirchhoff-approximate generalized Radon transform imaging using teleseismic P-to-S scattered waves. *Geophysical Journal International*, *192*, 1196–1216.

Miller, D., Oristaglio, M., & Beylkin, G. (1987). A new slant on seismic imaging: Migration and integral geometry. *Geophysics*, *52*, 943–964.

Papanikolaou, D. J., & Royden, L. H. (2007). Disruption of the hellenic arc: Late miocene extensional detachment faults and steep pliocene-quaternary normal faults—Or what happened at corinth? *Tectonics*, *26*, TC5003. https://doi.org/10.1029/2006TC002007

Park, J., & Levin, V. (2000). Receiver functions from multiple-taper spectral correlation estimates. *Bulletin of the Seismological Society of America*, *90*, 1507–1520.

Pavlis, G. L. (2011). Three-dimensional, wavefield imaging of broadband seismic array data. *Computers and Geosciences*, *37*, 1054–1066.

Pe-Piper, G., & Piper, DavidJ. W. (2007). Neogene backarc volcanism of the aegean: New insights into the relationship between magmatism and tectonics. *Geological Society of America*, *418*, 17–31.

Pearce, F. D., Rondenay, S., Sachpazi, M., Charalampakis, M., & Royden, L. H. (2012). Seismic investigation of the transition from continental to oceanic subduction along the Western Hellenic Subduction Zone. *Journal of Geophysical Research*, *117*, B07306. https://doi.org/10.1029/2011JB009023

Phinney, R. A. (1964). Structure of the Earth's crust from spectral behavior of long-period body waves. *Journal of Geophysical Research*, *69*, 2997–3017.

Rondenay, S. (2006). Multi-disciplinary experiments for dynamic understanding of subduction under the aegean sea. *International Federation of Digital Seismograph Networks*. https://doi.org/10.7914/SN/XS_2006

Rondenay, S. (2009). Upper mantle imaging with array recordings of converted and scattered teleseismic waves. *Surveys in Geohpysics*, *30*, 377–405.

Rondenay, S., Bostock, M. G., & Fisher, K. M. (2005). Multichannel inversion of scattered teleseismic body waves: Practical considerations and applicability. *Geophysical Monograph Series*, *157*, 2–17.

Rondenay, S., Bostock, M. G., & Shragge, J. (2001). Multiparameter two-dimensional inversion of scattered teleseismic body waves: 3. Application to the cascadia 93 data set. *Journal of Geophysical Research*, *106*, 30,795–30,807.

Rondenay, S., Montési, LaurentGJ, & Abers, G. A. (2010). New geophysical insight into the origin of the Denali volcanic gap. *Geophysical Journal International*, *182*, 613–630.

Rondenay, S., Spieker, K., Sawade, L., Halpaap, F., & Farestveit, M. (2017). Glimer: A new global database of teleseismic receiver functions for imaging earth structure. *Seismological Research Letters*, *88*, 1–10.

Ryberg, T., & Weber, M. (2000). Receiver function arrays: A reflection seismic approach. *Geophysical Journal International*, *141*, 1–11.

Schimmel, M., & Paulssen, H. (1997). Noise reduction and detection of weak, coherent signals through phase-weighted stacks. *Geophysical Journal International*, *130*, 497–505.

Shang, X., de Hoop, M. V., & van der Hilst, R. D. (2017). Common conversion point stacking of receiver functions versus passive-source reverse time migration and wavefield regularization. *Geophysical Journal International*, *209*, 923–934.

Sheehan, A. F., Shearer, P. M., Gilbert, H. J., & Dueker, K. G. (2000). Seismic migration processing of P-SV converted phases for mantle discontinuity structure beneath the Snake River Plain, western United States. *Journal of Geophysical Research*, *105*, 19,055–19,065.

Tauzin, B., Bodin, T., Debayle, E., Perrillat, J.-P., & Reynard, B. (2016). Multi-mode conversion imaging of the subducted Gorda and Juan de Fuca plates below the North American Continent. *Earth and Planetary Science Letters*, *440*, 135–146.

Tauzin, B., Reynard, B., Perrillat, J.-P., Debayle, E., & Bodin, T. (2017). Deep crustal fracture zones control fluid escape and the seismic cycle in the Cascadia subduction zone. *Earth and Planetary Science Letters*, *460*, 1–11.

Tessmer, G., & Behle, A. (1988). Common reflection point data-stacking technique for converted waves. *Geophysical Prospecting*, *36*, 671–688.

Tonegawa, T., Hirahara, K., Shibutani, T., Iwamori, H., Kanamori, H., & Shiomi, K. (2008). Water flow to the mantle transition zone inferred from a receiver function image of the Pacific slab. *Earth and Planetary Science Letters*, *274*, 346–354.

Tromp, J., Komatitsch, D., & Liu, Q. (2008). Spectral-element and adjoint methods in seismology. *Communications in Computational Physics*, *3*, 1–32.

Tzanis, A., Efstathiou, A., Chailas, S., & Stamatakis, M. (2018). Evidence of recent plutonic magmatism beneath northeast Peloponnesus (Greece) and its relationship to regional tectonics. *Geophysical Journal International*, *212*, 1600–1626.

Wang, Y., & Pavlis, G. L. (2016). Roughness of the mantle transition zone discontinuities revealed by high-resolution wavefield imaging. *Journal of Geophysical Research: Solid Earth*, *121*, 6757–6778. https://doi.org/10.1002/2016JB013205

Wilson, D., & Aster, R. (2005). Seismic imaging of the crust and upper mantle using regularized joint receiver functions, frequency-wave number filtering and multimode Kirchhoff migration. *Journal of Geophysical Research*, *110*, B05305. https://doi.org/10.1029/2004JB003430

Wu, R., & Aki, K. (1985). Scattering characteristics of elastic waves by an elastic heterogeneity. *Geophysics*, *50*, 582–595.

Yamauchi, M., Hirahara, K., & Shibutani, T. (2003). High resolution receiver function imaging of the seismic velocity discontinuities in the crust and the uppermost mantle beneath southwest Japan. *Earth, Planets, Space*, *55*, 59–64. https://doi.org/10.1186/bf03352463

Ylmaz, O. (2001). Seismic data analysis.

Zheng, Y., Lay, T., Flanagan, M. P., & Williams, Q. (2007). Pervasive seismic wave reflectivity and metasomatism of the tonga mantle wedge. *Science*, *316*, 855–859.